

Electrical Interconnects for Silicon Spin Qubits

Christopher David White,^{1,*} Anthony Sigillito,² and Michael J. Gullans^{1,†}

¹*Joint Center for Quantum Information and Computer Science,
NIST/University of Maryland, College Park, MD 20742, USA*

²*Department of Electrical and System Engineering,
University of Pennsylvania, Philadelphia, Pennsylvania 19104, USA*

Scalable spin qubit devices will likely require long-range qubit interconnects. We propose to create such an interconnect with a resistive topgate. The topgate is positively biased, to form a channel between the two dots; an end-to-end voltage difference across the nanowire results in an electric field that propels the electron from source dot to target dot. The electron is momentum-incoherent, but not necessarily spin-incoherent; we evaluate threats to spin coherence due to spin-orbit coupling, valley physics, and nuclear spin impurities. We find that spin-orbit coupling is the dominant threat, but momentum-space motional narrowing due to frequent scattering partially protects the electron, resulting in characteristic decoherence lengths ~ 15 nm for plausible parameters.

I. INTRODUCTION

Silicon spin qubits [1–3] offer a promising platform for scalable quantum computation, due to existing fabrication infrastructure and the small size of the physical qubits. Recent experiments have demonstrated high-fidelity state preparation, readout, and single- and two-qubit gates [4–8]. But silicon spin qubits require dense control electronics, which constrain both device layouts and high-level properties like qubit connectivity. Moreover, both NISQ calculations [9] and many quantum error correcting codes [10] benefit from long-range gates.

A large-scale spin qubit device will therefore require not only good qubits, but also medium and long-range interconnects between qubits [11, 12]. Existing proposals for interconnects include adiabatic passage through an array of quantum dots [13–20], bucket-brigade shuttling [21–30], conveyor-mode shuttling [11, 31–34], coupling to microwave cavities [35–43], and more [44–47]. In bucket-brigade interconnects, the electron undergoes coherent adiabatic shuttling through a sequence of dots, controlled by precise modulations of barrier and accumulator gate potentials. Conveyor-mode devices avoid some limitations of bucket-brigade shuttling. Rather than passing through Landau-Zener transitions from dot to dot, an electron in a conveyor-mode interconnect travels in a moving potential created by many gates with relatively few control lines; the electron speed is a few meters per second. In microwave interconnects, qubits are coupled to a microwave resonator, leading to effective two-qubit gates between qubits separated by distances up to millimeters.

We propose to shuttle electrons between dots separated by distances $L \sim 100$ μm using a single nanowire as a resistive topgate (Fig. 1). The topgate is positively biased, to form a channel between the two dots; an end-to-end voltage difference across the nanowire results in

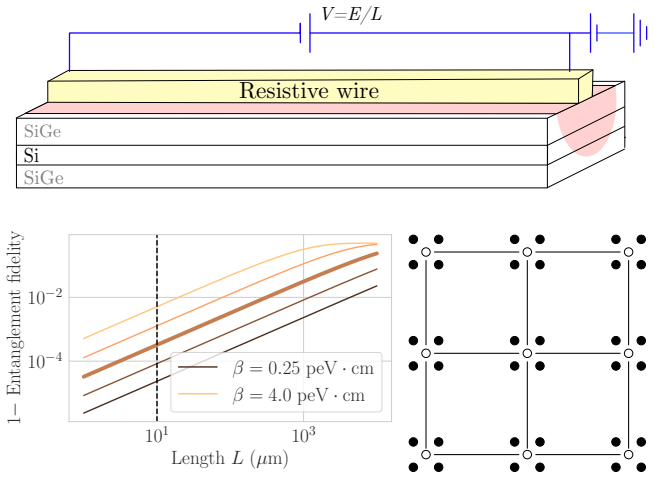


FIG. 1. **Top: proposed device.** A Si/SiGe heterostructure confines an electron to the thin Si layer. A resistive topgate creates a one-dimensional channel in the Si layer, and generates an electric field along the channel; an electron in the channel undergoes momentum-incoherent but spin-coherent transport down the channel. **Bottom left: entanglement fidelity** of transport across the channel as a function of channel length and spin-orbit interaction. Spin-orbit interaction couples the electron’s spin degree of freedom to its momentum degree of freedom, which is incoherent due to scattering. Momentum-space motional narrowing, caused by frequent scattering, partially protects the spin degree of freedom. The bold line shows Dresselhaus spin-orbit coupling $\beta = 1$ $\text{peV} \cdot \text{cm}$, the value we expect for our devices (cf App. A.1.) **Bottom right:** a potential architecture using interconnects to connect plaquettes of five dots, four filled (filled circles) and one empty (empty circle).

an electric field that propels the electron from source dot to target dot. We assume that the electron is scattered by phonons, conduction electrons in the wire, and other inelastic scattering sources, so that it can move from the source dot to the lower-energy target dot without heating up. We also assume that this scattering can be treated in a Drudé-like picture, implicitly resting on a Boltzmann

* christopher.d.white117.ctr@us.navy.mil

† mgullans@umd.edu

Si thickness	b	10 nm
Channel width	w	100 nm
Channel length	L	100 μm
Temperature	T	30 mK
Electric field in channel	E	1 V/cm
Zeeman field	B	0.5 T
Spin-orbit coupling (Rashba)	α	0.2 peV \cdot cm
(Dresselhaus)	β	1 peV \cdot cm
Intervalley g -factor variation	$\delta g/g$	10^{-4}
Mobility	μ	100,000 $\text{cm}^2/\text{V} \cdot \text{s}$
^{29}Si concentration		800 ppm

TABLE I. **Model device parameters:** except where specified, we take the device to have these parameters. For the spin-orbit coupling, see App. A.1; for the intervalley g -factor variation see [54].

equation for populations in momentum states.

The shuttling process is necessarily momentum-incoherent, but we expect it to be spin-coherent. Momentum scattering does not directly threaten spin coherence because many sources of scattering (e.g. phonons or oxygen impurities [48]) do not directly couple to the spin. But other effects do threaten spin coherence (Fig. 2). The spin is coupled to the momentum via spin-orbit coupling, so the momentum will gradually thermalize the spin [49–51]; the g -factor varies in space through the channel; diabatic transitions between the electron’s two valley states give a fluctuating g -factor; and nuclear spin impurities can flip or dephase the spin. We estimate the effect of these noise sources on transport (but not tunneling between dot and channel). We find that nuclear spin impurities and valley effects are made negligible by motional narrowing. Spin-orbit coupling to the momentum, therefore, is likely to be the dominant effect; if the spin-orbit coupling coefficients are comparable to those measured [52] and simulated [53] in Si/SiGe heterostructures, it will result in fidelities ~ 0.996 for a 100 μm channel.

The paper is organized as follows. In Sec. II we describe the proposed device and our model of the moving electron’s dynamics, and in Sec. III we summarize our results. In Sec. IV we describe the effect of spin-orbit coupling, in Sec. V we describe valley effects, in Sec. VI we consider spatial variation in the g -factor, and in Sec. VII we describe nuclear spin impurities. We conclude in Sec. VIII by summarizing our assumptions and results, outlining experiments which test those assumptions, and describing some potential applications of the device.

II. DEVICE

We consider a layered Si/SiGe heterostructure (Fig. 1 top), with electrons confined to a $b = 10$ nm layer of Si isotopically enriched to 800 ppm ^{29}Si . On top of the

Momentum relaxation time	$\tau_k = \mu m_t/e$	11 ps
Larmor freq. (angular)	$\Omega = g\mu_B B/\hbar$	88 GHz
Larmor freq. (rotational)	$g\mu_B B/(2\pi\hbar)$	14 GHz
Electron Larmor period	$2\pi\hbar/(g\mu_B B_z)$	71 ps
Average electron speed	$v_0 = \mu E$	10^3 m/s
Average electron momentum	$k_0 = \mu m E/\hbar$	$1.6 \mu\text{m}^{-1}$
Variance of electron momentum	$\langle \delta k^2 \rangle = \frac{mT k_B}{\hbar^2}$	$(2.5 \mu\text{m}^{-1})^2$
Spin-orbit coupling length	$\hbar^2/m_t\beta$	40 μm
Spin-orbit coupling velocity	β/\hbar	15 m/s
Time across 100 μm interconnect	T_{cross}	100 ns

TABLE II. **Derived device parameters** (cf Table I). In this table we write \hbar, k_B explicitly; in many symbolic expressions elsewhere in the paper we take $\hbar = k_B = 1$.

device are accumulator gates, barrier gates, and a resistive topgate. These gates form two quantum dots connected by a long channel, formed by biasing the resistive topgate; each dot is separated from the channel by a barrier controlled by a barrier gate. The channel is narrow ($w = 100$ nm), so orbital excitations in the plane of the quantum well but perpendicular to the wire are gapped out by $\sim \hbar^2/2mw^2 \approx 20\mu\text{eV}$ or a temperature of ~ 230 mK, larger than our model device temperature of 30 mK. We therefore take the channel is effectively one-dimensional, though future, more detailed calculations may need to take into account orbital excitations. Table I gives the device parameters we use; Table II gives certain derived quantities.

The resistive topgate also induces an electric field along the channel. It is convenient to imagine tuning the electric field E down the channel, rather than the potential difference between dots—if we imagined tuning the potential difference, we would introduce a spurious length dependence.

Electrons in the silicon forming the quantum dots and the channel have a band structure with six conduction-band minima, or valleys, in the $\pm x, y, z$ directions. Strain effects raise the energy of the $\pm x, y$ valleys by meV, so they are negligible, leaving the z valley states; the z valley states are split by the combined effect of the interface and the confining electric potential of the topgate [2, 3]. We therefore consider a one-dimensional effective model for the momentum and valley degrees of freedom

$$H_{\text{mom}} = -\frac{\hbar^2 k_x^2}{2m_t} + \Delta(x)[\tau^x \cos \phi(x) + \tau^y \sin \phi(x)], \quad (1)$$

where $m_t = 0.19m_e$ is the transverse effective mass of the electron, $\tau^{x,y}$ are Pauli matrices in valley space, and $\Delta(x)$ and ϕ are the the position-dependent valley splitting and phase [55].

The electron is strongly scattered, resulting in a momentum correlation time $\tau_k = \mu m_t/e$, μ the mobility; we take this to be described broadly by the Drudé model. We assume the scattering is primarily inelastic. Inelastic scattering requires scattering mechanisms other than

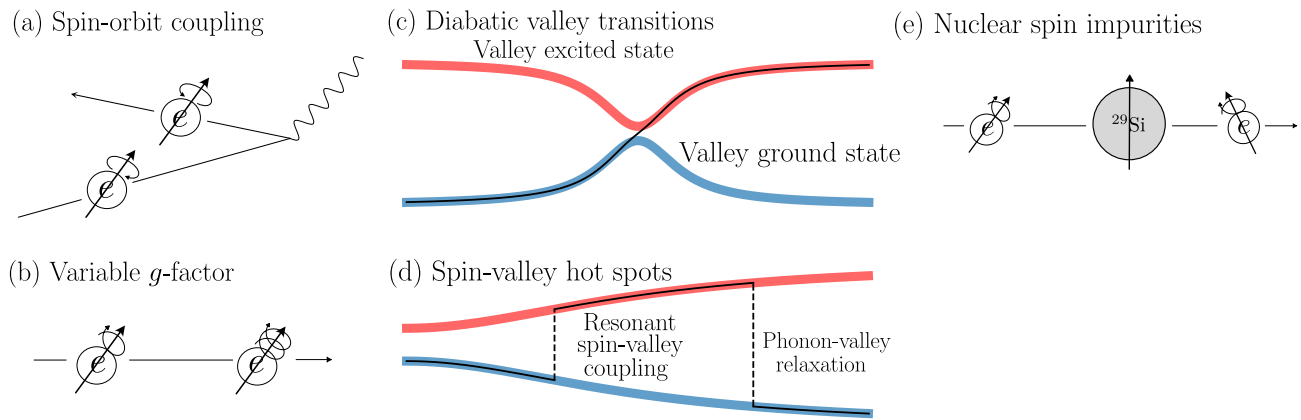


FIG. 2. **Sources of decoherence.** (a) **Spin-orbit coupling:** as the electron scatters, the effective field due to spin-orbit coupling changes randomly. We find that this is the dominant source of decoherence. (b) **Valley-dependent g -factor:** The valley splitting has a large random component, due to (e.g.) alloy disorder at the interface, so sometimes it is small. At points where it is small, the electron can diabatically transition to an excited state, which has a slightly different g factor. (c) **Spin-valley hotspots:** When the valley splitting is on resonance with the Zeeman field, spin-valley coupling can flip both spin and valley; later spin-independent valley relaxation (e.g. due to phonons) brings the electron back to the valley ground state, now in a different spin state. (d) **Nuclear spin impurities:** As the electron passes near the rare spin-1/2 ^{29}Si , hyperfine interaction with the ^{29}Si nuclear spin can change the electron spin.

the impurities discussed in [48, 56]—perhaps excitation of phonons or scattering from conduction electrons in the resistive topgate. Some degree of inelastic scattering is crucial to our scheme, because the electron starts at high energy at one end of the channel and ends at low energy at the other end of the channel; it also justifies our Drudé picture of transport. If impurities are in fact the dominant scattering mechanism in our system, the electron will Anderson localize, and electron transport will be better treated in terms of Mott variable-range hopping between Anderson eigenstates [57–59]; we leave that regime to future work.

The electron is in a Zeeman field B ; we take B to be oriented along the channel, i.e. the x axis. This gives a Hamiltonian term

$$H_B = \frac{1}{2}\mu_B[g + g'(x) + (\delta g)(\tau^x \cos \phi + \tau^y \sin \phi)]B\sigma^x. \quad (2)$$

$g'(x)$ gives the (random) spatial variation of the g -factor. (Although this spatial dependence results from variation in the spin-orbit coupling coefficients, it is convenient to treat it separately from the spin-orbit coupling to the incoherent momentum state). δg encodes the valley dependence of the g -factor, which we discuss in Sec. V; in that section we also briefly discuss the effect of spatially-varying g factors, as well as valley hot spots.

The Si/SiGe interface gives a spin-orbit coupling

$$H_{\text{SOC}} = k_x(\alpha\sigma^y + \beta\sigma^x). \quad (3)$$

(In principle it also leads to terms $k_y[\alpha\sigma^x + \alpha\sigma^y]$, but because the electron is in a coherent k_y state, these terms will not lead to irreparable loss of fidelity.) The valley dependence of the spin-orbit coupling does not affect the

decoherence, as we discuss in Sec. V.1.) We assume that the momentum degree of freedom relaxes to a Gibbs state

$$\rho_{\text{momentum}} = Z^{-1} \exp \left[-\frac{\hbar^2}{2m_t k_B T} (k - k_0)^2 \right], \quad (4)$$

where $k_0 = mE\mu/\hbar$ is the drift momentum. (This is in contrast to [60], which treats conveyor-mode shuttling and so assumes that the electron is always in a coherent position state.) Eq. (4) can be understood as the maximum-entropy state subject to energy and average-momentum constraints.

We are agnostic as to the details of the scattering process. Instead of considering those details, we use a phenomenological momentum correlation function. We take that correlation function to have single-time variance $\langle (k - k_0)^2 \rangle = m_t k_B T / \hbar^2$, in accordance with (4), and a correlation time $\tau_k = \mu m_t / e$. We do assume that the scattering process is inelastic, and in fact thermalizes the electron with the scattering source, so the electron's temperature does not increase as it travels down the wire.

We assume that ^{29}Si nuclear spin impurities are uniformly distributed at a density of 800 ppm [61] throughout the slice of silicon in which the electron travels. (We ignore the ^{73}Ge nuclear spins.) We take the nuclear spins to be at infinite temperature. These nuclear spins interact with the electron via a contact hyperfine interaction, which we treat in scattering theory.

Source	Relaxation L_1	Decoherence L_2	Infidelity at 100 μm
Spin-orbit coupling	$\frac{4m_t^2 k_B T}{\hbar^4 e E} \frac{\alpha^2}{1 + (\Omega \tau_k)^2} \approx 0.74 \text{ m}$	$\frac{2m_t^2 k_B T}{\hbar^4 e E} \left(2\beta^2 + \frac{\alpha^2}{1 + (\Omega \tau_k)^2} \right) \approx 1.5 \times 10^{-2} \text{ m}$	3.2×10^{-3}
Valley-dependent spin-orbit	(subsumed by valley-independent SOC)		
Valley-dependent g -factor		$\sim (\Omega \delta g / g)^2 (\zeta / v^2) \sim 1 \times 10^{-1} \text{ m}$	5×10^{-4}
Spin-valley hot spots	1 m		5×10^{-5}
Spatial g -factor variability		2 m	2×10^{-5}
Nuclear spin impurities		$1 \times 10^5 \text{ m}$	3×10^{-10}

TABLE III. **Summary of contributions to infidelity** and relaxation (L_1) and decoherence (L_2) lengths. Numerical results use the model device parameters of Table I. Spatial g -factor variability and valley-dependent g -factor lead only to decoherence; likewise, spin-valley hotspots lead only to relaxation. Although nuclear spins cause both relaxation and decoherence, we only estimate decoherence; we expect relaxation to be an even smaller effect. $\Omega = \mu_B B g / \hbar$ is the (angular) Larmor frequency, $\tau_k = \mu m_t / e$ the momentum scattering time, ζ the distance between points of small valley splitting.

III. SUMMARY OF RESULTS

III.1. Relaxation and decoherence lengths; Kraus operators

Qubit performance can be characterized by timescales for spin relaxation (T_1) and dephasing (T_2). For an interconnect the parameter of interest is not a dwell time but the interconnect length. We therefore frame our results in terms of lengthscales for spin relaxation (L_1) and dephasing (L_2):

$$\begin{aligned} \langle \sigma^x \rangle &\propto e^{-L/L_1} \\ \langle \sigma^{y,z} \rangle &\propto e^{-L/L_2} \end{aligned} \quad (5)$$

(recall that our quantization axis is the x axis). We consider decoherence due to spin-orbit coupling, valley-dependent g -factor, spin-valley hot spots, spatial g -factor variation, and nuclear spin impurities. Fig. 2 shows sketches of these processes; Table III shows their L_1 , and L_2 , as well as contributions to the entanglement fidelity (vide infra).

We find that both relaxation and decoherence are dominated by the D'yakonov-Perel' effect, i.e. spin-orbit coupling to the incoherent momentum. The resulting lengths are

$$\begin{aligned} \frac{1}{L_1} &= \frac{4m_t^2 k_B T}{eE} \frac{\alpha^2}{1 + (\mu_B B g \mu m_t / \hbar e)^2} \\ \frac{1}{L_2} &= \frac{2m_t^2 k_B T}{eE} \left(2\beta^2 + \frac{\alpha^2}{1 + (\mu_B B g \mu m_t / \hbar e)^2} \right); \end{aligned} \quad (6)$$

for the model device parameters of Table I, these are

$$\begin{aligned} L_1 &\approx 74 \text{ cm} \\ L_2 &\approx 15 \text{ mm}. \end{aligned} \quad (7)$$

For reasonable parameters the valley-dependent g -factor gives an L_2 length ~ 10 cm, longer than the SOC L_2 (Sec. V.1); the effects of valley hot spots (Sec. V.2) and nuclear spin impurities (Sec. VII) are much smaller still.

The resulting quantum channel has Kraus operators

$$\begin{aligned} K_1 &= a\sigma^- \\ K_2 &= f(bP_\uparrow + P_\downarrow) \\ K_3 &= d(bP_\uparrow - P_\downarrow). \end{aligned} \quad (8)$$

with

$$\begin{aligned} a &= \sqrt{1 - e^{-L/L_1}} \\ b &= \sqrt{e^{-L/L_1}} \\ d &= \sqrt{\frac{1}{2} (1 - e^{-L/L_2})} \\ f &= \sqrt{\frac{1}{2} (1 + e^{-L/L_2})}. \end{aligned} \quad (9)$$

III.2. Entanglement fidelities and spin blockade

The *entanglement fidelity* [62, 63] of a quantum channel \mathcal{E} is the fidelity of the channel, when applied to one half of a maximally entangled state. In our case, write $|\Omega\rangle$ for a singlet state; the entanglement fidelity is

$$F_e(\varepsilon) = \langle \Omega | (I \otimes \mathcal{E})(|\Omega\rangle\langle\Omega|) | \Omega \rangle; \quad (10)$$

it is related to the average of the channel fidelity between single-qubit gates

$$F_{\text{Haar}}(\mathcal{E}) = \int_{\psi \in \text{Haar}} d\psi \langle \psi | \mathcal{E}(|\psi\rangle\langle\psi|) | \psi \rangle \quad (11)$$

by

$$F_{\text{Haar}}(\mathcal{E}) = \frac{dF_e(\mathcal{E}) + 1}{d + 1}, \quad (12)$$

$d = 2$ the onsite Hilbert space dimension (see e.g. [64, Ex. 48])

The entanglement fidelity of the channel with the

Kraus operators of Eq. (8) in the previous section is

$$\begin{aligned} F_e &= \frac{1}{4} \sum_j \left(\text{Tr} K_j \right)^2 \\ &= \frac{1}{2} \left(1 + e^{-L/L_2} \right) e^{-L/2L_1} + \frac{1}{4} \left(1 - e^{-L/2L_1} \right)^2. \end{aligned} \quad (13)$$

In the limit of long relaxation and decoherence lengths, F_e reduces to

$$F_e = 1 - \frac{L}{2L_2} - \frac{L}{2L_1} + O[(L/L_{1,2})^2]. \quad (14)$$

IV. SPIN-ORBIT COUPLING

The spin-orbit coupling term (3) in the Hamiltonian couples the momentum, which is in an incoherent Gibbs state, to the spin state we seek to transport; this results in relaxation and decoherence due to the D'yakonov-Perel' effect [49–51]. The momentum has a scalar average k_0 and a fluctuating part δk , so the Zeeman and spin-orbit coupling parts of the spin Hamiltonian are

$$\begin{aligned} H &= \dots + \frac{1}{2} g \mu_B B \sigma^x + k_0 (\alpha \sigma^y + \beta \sigma^x) \\ &\quad + \delta k (\alpha \sigma^y + \beta \sigma^x) + \dots \end{aligned} \quad (15)$$

The first term is coherent, so we assume it can be corrected by a calibrated rotation after the electron reaches the target dot. The second term, however, results in a combination of spin relaxation and dephasing. The magnitude of this effect is controlled by the variance of the momentum $\langle \delta k^2 \rangle = m_t T$; the value of the spin-orbit coupling coefficients α, β , which we expect to be of order $\alpha \sim 0.2 \text{ peV} \cdot \text{cm}$, $\beta \sim 1 \text{ peV} \cdot \text{cm}$ (cf App. A.1); and the momentum correlation time τ_k given by the mobility.

We model the effect of spin-orbit coupling by treating the spin degree of freedom as our system of interest, and the momentum degree of freedom—together with all the scattering sources (impurities, phonons, conduction electrons, etc.)—as the bath.

The rate of relaxation and dephasing depend on the distribution of the momentum fluctuations δk . We take k to have a single-time distribution given by the Gibbs state (4), so $\delta k = k - k_0$ is Gaussian

$$p(\delta k) = Z^{-1} \exp \left[-\frac{\hbar^2}{k_B T} \frac{\delta k^2}{2m_t} \right]; \quad (16)$$

the single-time variance is $\langle \delta k^2 \rangle = m_t k_B T / \hbar^2$. For convenience and definiteness, we take the momentum to have exponential correlations

$$\langle \delta k(t') \delta k(t) \rangle = \langle \delta k^2 \rangle e^{-|t' - t| / \tau_k} \quad (17)$$

with correlation time given by the momentum relaxation time

$$\tau_k = \mu m_t / e. \quad (18)$$

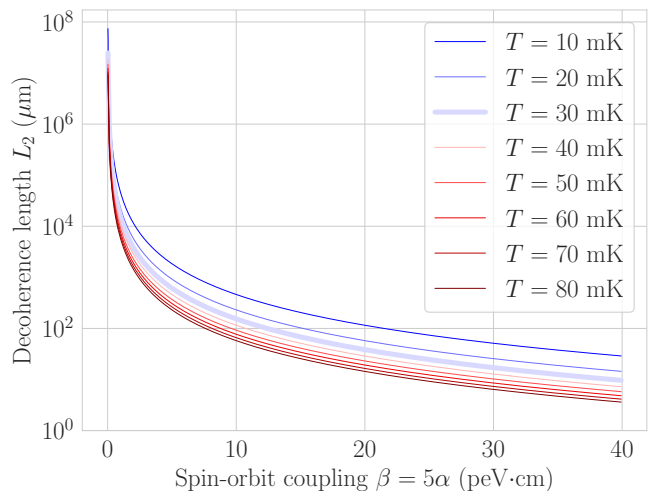


FIG. 3. **Decoherence lengths due to spin-orbit coupling** across electron temperatures. The decoherence length is approximately mobility-independent. Because we take the Zeeman field to be along the interconnect, the effective Dresselhaus field is parallel to the quantization axis and decoherence dominates; were we to take the Zeeman field perpendicular to the interconnect, the effective Dresselhaus field would still dominate, but would then cause relaxation of approximately the same magnitude.

We modify the resulting correlation function to satisfy the KMS relations [65–67], which are a necessary feature of correlation functions of Hamiltonian systems in thermal equilibrium. (A careful consideration of scattering processes would likely further modify the correlation function (17), but most of those effects are captured by the phenomenological correlation time τ_k of (18). As long as the correlations have that timescale, we do not expect our results to change by more than an $O(1)$ factor.) We give details of the resulting correlation function, together with the derivation of the Lindblad equation, in App. A.2, and a brief discussion of the KMS relation in App. A.3

On timescales long compared with τ_k , the average dynamics can be approximated by Lindblad evolution

$$\begin{aligned} d_t \rho &= \Gamma_{1-} \left(\sigma^- \rho \sigma^+ + \frac{1}{2} \{ \sigma^+ \sigma^-, \rho \} \right) \\ &\quad + \Gamma_{1+} \left(\sigma^+ \rho \sigma^- + \frac{1}{2} \{ \sigma^- \sigma^+, \rho \} \right) \\ &\quad + \Gamma_2 (\sigma^x \rho \sigma^x - \rho) \end{aligned} \quad (19)$$

with

$$\begin{aligned} \Gamma_{1-} &\approx \alpha^2 m k_B T \frac{4\tau_k}{1 + (\mu_B B g \tau_k / \hbar)^2} \\ \Gamma_{1+} &\approx \alpha^2 m k_B T \frac{4\tau_k}{1 + (\mu_B B g \tau_k / \hbar)^2} e^{-\Omega \hbar / k_B T} \\ \Gamma_2 &= 2m T \tau_k \beta^2 \end{aligned} \quad (20)$$

resulting in T_1 and T_2 rates

$$\frac{1}{T_1} \approx 4m_t k_B T \alpha^2 \frac{\tau_k}{1 + (\mu_B B g \tau_k / \hbar)^2} \quad (21a)$$

$$\frac{1}{T_2} \approx 2m_t k_B T \tau_k \left(2\beta^2 + \alpha^2 \frac{1}{1 + (\mu_B B g \tau_k / \hbar)^2} \right). \quad (21b)$$

(We have ignored Γ_{1+} , since it is suppressed by a factor $e^{-\Omega \cdot \hbar / k_B T}$ compared to the other rates.) For momentum scattering time $\tau_k \lesssim \hbar / \mu_B B g$ the Larmor precession time, both T_1 and T_2 increase as the scattering time decreases, i.e. as the mobility gets lower. This effect, already noted in [50], can be understood as motional narrowing in momentum space. The T_1 and T_2 of (21) lead to relaxation and decoherence lengths

$$\frac{1}{L_1} = \frac{1}{vT_1} = \frac{4m_t^2 k_B T}{eE} \frac{\alpha^2}{1 + (\mu_B B g \mu_t / \hbar e)^2} \quad (22)$$

$$\frac{1}{L_2} = \frac{1}{vT_2} = \frac{2m_t^2 k_B T}{eE} \left(2\beta^2 + \frac{\alpha^2}{1 + (\mu_B B g \mu_t / \hbar e)^2} \right)$$

Fig. 3 shows the decoherence length L_2 as a function of the spin-orbit coupling coefficients, across temperatures. (We use the model device values of Table I for other parameters.) Because the Dresselhaus spin-orbit coupling β is larger than the Rashba α and our magnetic field is parallel to the electron's motion, decoherence dominates. For the model device parameters of Table I we find

$$\begin{aligned} L_1 &\approx 0.74 \text{ m} \\ L_2 &\approx 15 \text{ mm} . \end{aligned} \quad (23)$$

When the momentum scattering time is $\tau_k \lesssim \hbar / (\mu_B B g)$ the Larmor precession time, the SOC relaxation and decoherence lengths are mobility-independent, because two countervailing effects cancel. As the mobility decreases the momentum scattering time decreases, leading to the momentum-space motional narrowing discussed above and longer T_1, T_2 . But as the mobility decreases, the speed decreases, so the time taken to travel any particular length increases.

The resulting quantum channel has Kraus operators of the same form as Eq. (8). The entanglement fidelity reduces to Eq. (14) in the limit of long relaxation and decoherence lengths.

V. VALLEY EFFECTS

Bulk silicon has six conduction band minima, or valleys: one on each of the $\pm k_x, k_y, k_z$ axes. In 2D heterostructures the $\pm k_x, k_y$ valleys are gapped out by strain, with gaps of order meV [2, 3]. The remaining valleys, on the $\pm k_z$ axis, have a spatially varying energy difference, or ‘‘valley splitting’’. Typically the valley splitting is of order 10-100 μeV , comparable to the Zeeman energy, but [68] argues that under plausible assumptions it frequently passes through zero along the length of a device.

The valley degree of freedom can impair device performance by coupling to the electron spin, together with the magnetic field (a valley-dependent g -factor, varying in space) and electron momentum (valley-dependent spin-orbit coupling, also varying in space). If the electron is in a mixed valley state, the coupling between valley and spin can dephase the qubit. If the valley splitting—the energy difference between valley-space energy eigenstates—is near the Zeeman energy, the device is said to have a *valley hot spot*. At a valley hot spot, the valley states may hybridize with the spin states, making the qubit sensitive to charge noise¹ and phonon-induced relaxation [69–78]. We argue that the electron is moving too quickly for any of these effects to matter: motional narrowing makes the effect of valley-dependent spin-orbit coupling and g -factor negligible, and the electron spends too little time near valley hot spots to appreciably relax.

We do not consider valley-driven decoherence after the electron enters the target dot. If the electron enters the dot's valley-excited state, it may remain there for milliseconds [75], much longer than relevant gate times; during that period, the valley g -factor difference will give nontrivial decoherence.

Although the dot entry process requires further study, we expect that the probability for the electron to enter the dot valley-excited state will be thermally suppressed. We assume that the dot entry process will be inelastic, in the sense that it is driven by a process that exchanges energy with some other system (e.g phonon emission or scattering from wire electrons). Because that other system is at a temperature small compared to the likely target-dot valley splitting $\Delta_{\text{target}} \sim 100 \mu\text{eV}$, the inelastic transition process is much more likely to take the electron to the target dot's valley-ground state than to the valley-excited state. If the transition process is elastic the electron may end up in the target-dot valley-excited state. We expect that one could engineer intervalley relaxation, perhaps using a second dot.

V.1. Valley-dependent spin-orbit coupling and g -factor

The relevant terms in the Hamiltonian are

$$\begin{aligned} H = & \dots \\ & + \Delta(x) \tau^x \quad [\text{valley splitting}] \\ & + \frac{1}{2} \hbar \Omega \frac{\delta g}{g} \tau^x \sigma^x \quad [\text{valley-dependent } g] \\ & + k(\beta) \tau^x \sigma^x \quad [\text{valley-spin-orbit}] \\ & + \dots . \end{aligned} \quad (24)$$

¹ Typically, the valley states are in slightly different positions: see e.g. [54], so they couple slightly differently to charge noise. When the valley states hybridize with the spin states, then, the spin states also couple slightly differently to charge noise, leading to decoherence.

where $\tau^{x,y,z}$ are valley-space Pauli operators.² We do not consider valley-dependent Rashba spin-orbit coupling; in effective-mass fits to experimental data, the valley-dependent part of the Rashba coupling is much smaller than the Dresselhaus coupling, which is largely valley-dependent [54].

To estimate the effect of valley-dependent couplings, we assume that the electron passes diabatically through many places where $\Delta(x)$ is small, leading to a random valley state. We assume that small valley splittings occur with density ζ^{-1} and treat the valley degree of freedom as classical telegraph noise with switching rate ζ/v . We ignore spatial variation in the coupling constants between valley and spin.³

The correlation time of the valley state is

$$\tau_v \sim \zeta/v_0. \quad (25)$$

For $\zeta = 100$ nm (cf [68, 79]) and $v_0 = 1000$ m/s, this is $\tau_v \sim 100$ ps $\gg \tau_k \sim 10$ ps the momentum correlation time, so the effect of Dresselhaus spin-orbit coupling in dephasing the qubit is controlled by the momentum correlation time, not the valley-space correlation time, even though the Dresselhaus spin-orbit coupling is strongly valley-dependent. This is why we treated the Dresselhaus spin-orbit-coupling above in Sec. IV, rather than here.

Using the valley correlation time $\tau_v \sim \zeta/v_0$, then, the dephasing rate is

$$1/T_2 \sim \left(\Omega \frac{\delta g}{g} \right)^2 (\zeta/v_0) \quad (26)$$

For reasonable parameters⁴ ($\zeta = 100$ nm [79], $\delta g/g = 10^{-4}$ [54]) this gives $T_2 \sim 100$ μ s or $L_2 \sim T_2 v \sim 10$ cm, much longer than the $L_2 \sim 15$ mm due to spin-orbit coupling.

² In fact the valley splitting rotates in the $\tau^{x,y}$ plane, as well as fluctuating in magnitude, but this rotation does not affect our estimates.

³ This assumption is justified if the correlation length of the coupling constants is not appreciably shorter than ζ , and if the coupling constants and the valley splitting are independent.

They may not be independent! Consider an interface step. [54] found the valley-dependent Dresselhaus spin-orbit coupling $\delta\beta$, and consequently the valley-dependent g factor δg , change signs at an interface step. But [55] find that under certain conditions the valley splitting has a minimum at an interface step. So the effects may cancel: the electron may pass diabatically through this valley-splitting minimum, leaving the minimum in the valley excited state—but this valley excited state has the same spin-orbit coupling as the previous valley ground state.

In fact interface steps are unlikely to produce valley minima. [55] finds that if the interface is more than a monolayer thick, the interface steps have a small effect on the valley splitting, which is dominated by alloy disorder, and (in this particular instance) our independence assumption not broken. Nonetheless our independence assumption is nontrivial, and may require reconsideration in future work.

⁴ The small-valley-splitting length ζ comes from experiments [79] with tightly localized electron wavefunctions. The effective valley splitting is the result of averaging over the valley disorder in

V.2. Valley hot spots

In a static dot the fixed valley splitting Δ may be close to the Zeeman frequency. If that is the case, and if there is a spin-valley coupling

$$H = \dots + \Delta\tau^z + J\tau^z\sigma^z + \dots \quad (27)$$

between the valley and spin, the two will hybridize. The spin is then subject to phonon-driven valley relaxation processes and charge noise. In dots the coupling has been measured at $J \sim 10$ MHz $\cdot \hbar \sim 40$ neV [80].

In a resistive interconnect Δ varies as it passes through different alloy disorder realizations and (potentially) interface steps. ([55] gives a helpful introduction to this physics.) If the electron wavepacket has a length scale l_e and a speed v_0 , the disorder changes on a timescale $\sim l_e/v_0$; if the valley splitting Δ has a standard deviation σ_Δ , its rate of change is

$$\frac{d\Delta}{dt} \sim \sigma_\Delta v_0 / \hbar l_e. \quad (28)$$

The spin and valley can only hybridize if

$$|\Delta - g\mu B| \lesssim J \quad (29)$$

for a time $t_{hs} \gtrsim J/\hbar$. This timescale is

$$t_{hs} \sim J \left[\frac{d\Delta}{dt} \right]^{-1} \sim \frac{J l_e}{\sigma_\Delta v_0}. \quad (30)$$

The degree of hybridization, then, is roughly

$$p \sim \lambda t_{hs} \sim \frac{J^2 l_e}{\hbar \sigma_\Delta v_0}; \quad (31)$$

if this is small then the electron passes through the valley hot spot too rapidly for spin-valley relaxation or valley-mediated charge noise to affect it.

Assume the electron wavepacket has a length scale $l_e \sim 1$ μ m, and the standard deviation of Δ is $\sigma_\Delta \sim 10$ μ eV. Then $t_{hs} \sim 0.7$ ps and $J t_{hs} / \hbar \sim 7 \cdot 10^{-6}$. We can heuristically estimate a hot-spot driven relaxation length. Assume that every time the electron passes through a hot spot, its spin state goes to the ground state with probability $p \sim J t_{hs} / \hbar$. The probability that any particular location is a hot spot is $p_{hs} \lesssim J / \sigma_\Delta$, so the linear density of hot spots is $\lambda_{hs} \sim J / \sigma_\Delta l_e$ and the relaxation length is

$$\frac{1}{L_1} \sim p \lambda_{hs} \sim \frac{J^3}{\sigma_\Delta^2 \hbar v_0} \sim (1 \text{ m})^{-1} \quad (32)$$

the whole area of the wavefunction, so passing from the tightly localized wavefunctions of [79] to the extended wavefunctions of our device will change the valley-splitting disorder parameters. If the valley splitting turns out to be an important source of dephasing, this will require more careful consideration. As it is, we do not expect the resulting change in parameters to change our conclusion that valley effects are less important than spin-orbit coupling.

This is comparable to the spin-orbit-driven relaxation length $L_1 \approx 0.74$ cm (for our model device parameters), so—depending on the constant factors and the parameters of the actual device—valley hot spots may in fact control spin relaxation. But it is much longer than the spin-orbit-driven decoherence length scale $L_2 \approx 15$ mm, so hot spots are unlikely to control device performance.

VI. SPATIALLY-VARYING g -FACTOR

Because the g -factor has a contribution from spin-orbit coupling it varies slightly with alloy disorder, interface steps, and other random effects. As the electron passes through the interconnect, then, it experiences a variable g -factor.⁵ The resulting evolution has both a deterministic component and a variable component. If the electron's path were deterministic, the resulting total z rotation would be the same shot-to-shot, and could be corrected. But in fact the electron travels diffusively through the channel, so the path (i.e. the time spent in each region) varies from shot to shot.⁶

In App. B we give a detailed calculation. In this section we review the assumptions of that calculation (essentially, that electron wavepackets travel in a directed random walk) and give a heuristic derivation of the resulting decoherence length.

Consider an electron in a coherent wavepacket of some length l_e , and assume it travels down the wire in a directed random walk. The electron coherence length l_e is a key parameter of the calculation, but—because it depends on the details of the scattering—it is difficult to estimate. The coherence length must be longer than the scattering length $\tau_k v_0 \sim 10$ nm; we expect it to be longer than typical dot length scales, $l_e \gg 100$ nm. We take the directed random walk to have diffusion constant $D = k_B T \mu / e \approx (160 \text{ nm})^2 / \text{ns}$ given by the Einstein relation, and drift velocity $v = \mu E \approx 1000$ m/s.

Because the wavepacket has length l_e and width w the channel width, the electron spin evolves under the average Larmor frequency in that area. If the variation in the local Larmor frequency is short-range correlated—e.g. because it comes from spin-orbit coupling variation due to alloy disorder—the effective Larmor frequency, averaged

over the $l_e \times w$ area of the wavepacket, has correlation length $l_c = 2l_e$ ⁷ and location-to-location or device-to-device variance

$$\sigma_\Omega^2 \sim \sigma_0^2 / (l_e w). \quad (33)$$

Here σ_0 is a device property which we can estimate from dot-to-dot g -factor variation

$$\sigma_0^2 \sim l_{\text{dot}}^2 [\Omega_0 \Delta g / g]^2 \approx (0.44 \text{ GHz} \cdot \text{nm})^2 \quad (34)$$

where $l_{\text{dot}} \approx 50$ nm is the length scale of the dots of the experiments we consider [81, 82], $\Omega_0 = g \mu_B B / \hbar = 88$ GHz is our typical (angular, not rotational) Larmor frequency, and we take $\Delta g / g = 10^{-4}$ (see App. B.1).

To estimate the decoherence length, let us imagine that the Larmor frequency is uniform within boxes of length l_c the Larmor frequency correlation length, but varies randomly between boxes. The time t_{box} the electron spends in a box is on average l_c / v_0 , but has variance

$$\text{var } t_{\text{box}} \sim D l_c / v_0^3. \quad (35)$$

To see this, note that at a time $t = l_c / v_0$ after it enters the left end of the box, the electron's average position is at the right end of the box, but the variance of the position is $\text{var } x(t) = D l_c / v_0$. Since—whatever its position—it is moving at roughly a speed v_0 , this means that the variance in its exit time is $\text{var } t_{\text{box}} = \frac{1}{v_0} \text{var } x(t)$, giving (35). (This implicitly assumes that $l_c \gg D / v$, the length scale characterizing when drift dominates diffusive spread.)

If we work in a rotating frame, so the average Larmor frequency is 0, then in the box near position x , the electron's spin state undergoes a σ^x rotation by an angle

$$\theta_{\text{box}} = t_{\text{box}} \Omega_x. \quad (36)$$

(Recall that we have taken x to be our quantization axis.) The shot-to-shot variance of this angle is

$$\text{var } \theta_{\text{box}} = \Omega_x^2 \text{var } t_{\text{box}} \sim \Omega_x^2 D l_c / v_0^3. \quad (37)$$

The variance of the rotation over the course of the channel, then, is

$$\text{var } \theta_{\text{channel}} = \sum_{\text{boxes}} \text{var } \theta_{\text{box}} \sim L \sigma_\Omega^2 D / v_0^3 \quad (38)$$

since the variances add and the Ω_x^2 average to σ_Ω^2 . From this we can read off a decoherence length

$$L_2 \sim \frac{v_0^3}{\sigma_\Omega^2 D} \approx \frac{e l_e w \mu^2 E^3}{k_B T \sigma_0^2}. \quad (39)$$

The more detailed calculation of App. B gives the same answer, including constant factors, at leading order in

⁵ Strictly speaking it will experience a variable g -factor tensor: that is, the magnetic field term will undergo small random rotations, as well as small variations in magnitude. We expect this effect to be of the same magnitude as, or even smaller than, the already-small effect of scalar g -factor variation, so we do not treat it in detail.

⁶ In addition, the variable g -factor will lead to small spin-dependent scattering, which may lead to further decoherence. We expect decoherence due to this effect to be smaller than other sources we consider, because it is second-order: it involves both the (small) spatial g -factor variation and some other source of decoherence, e.g. the spin-orbit coupling of Sec. IV or the spatially-varying g -factor itself.

⁷ The factor of 2 comes from a Gaussian integration; see App. B.

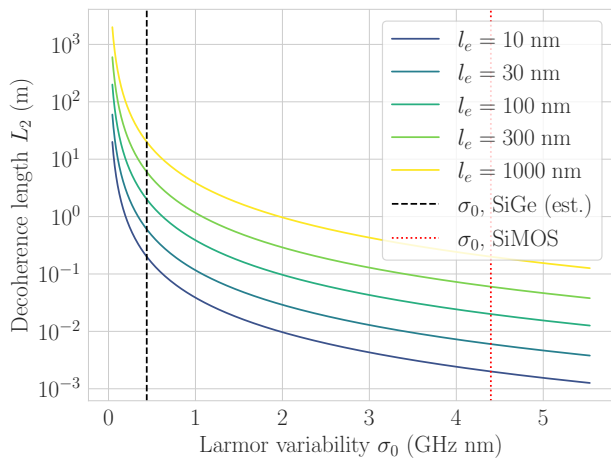


FIG. 4. **Decoherence length resulting from spatial g -factor variation**, across electron wavepacket lengths. Because the Larmor frequency variation is central-limiting, it is best understood as a standard deviation per unit length σ_0 . The red dotted line shows σ_0 corresponding to a dot-to-dot g factor variation $\Delta g/g = 10^{-3}$, consistent with SiMOS measurements [78]; the black dashed line shows a heuristic estimate for SiGe devices, corresponding to $\Delta g/g = 10^{-4}$.

$v_0/(Dl_e)$. In our case $v_0/D \sim 26$ nm and $l_e \gg 200$ nm, so this leading-order approximation is reasonable.

Fig. 4 shows this decoherence length as a function of σ_0 across wavepacket lengths l_e . Under pessimistic assumptions ($l_e = 10$ nm; $\sigma_0 \gtrsim 4$ GHz nm, consistent with SiMOS measurements) this gives a shorter L_2 than the spin-orbit coupling contribution we calculated for our model device parameters in Sec. IV. But pessimistic assumptions for the g -factor variability are in tension with the model device parameters: if the g -factor variability is large, we expect the spin-orbit coupling to be large. For our model device parameters and $l_e = 100$ nm, the g -factor decoherence length is $L_2 \sim 2$ m, much longer than the decoherence length due to spin-orbit coupling $L_2 \approx 15$ mm.

Both this heuristic calculation and the more detailed calculation of App. B make three major assumptions: that the Larmor frequency variation is short-range correlated; that the electron’s position state can be treated semiclassically, as a wavepacket with a center undergoing a directed random walk; and that the electron’s correlation length is long compared to the mean free path.

The Larmor frequency variation may not be short-range correlated. It may come from rare, widely-spaced interface steps, or it may come from magnetic field gradients. Interface steps, like alloy disorder, can change the spin-orbit coupling, hence the g -factor. In that case we expect the calculation to be broadly similar to the calculation we present here. If the typical step separation l_{step} is $l_{\text{step}} \ll l_e$, then the calculation here will be unchanged. If, however, the step separation is $l_{\text{step}} \gg l_e$, then the effective g -factor will not be central-limiting, so the σ_0^2 will have a different form, and in the expres-

sion (35) for $\text{var } t_{\text{box}} l_e$ will become l_{step} . If the Larmor frequency variation comes from inhomogeneities in the magnetic field, perhaps due to a micromagnet, the tools of App. B can still be used, but the calculation will differ substantially.

VII. NUCLEAR SPIN IMPURITIES

Although the atoms around the electron are primarily ^{28}Si , which has no nuclear spin, a few are ^{29}Si , which has nuclear spin 1/2. These nuclear spin impurities have a small gyromagnetic ratio, so their spin distribution is not appreciably modified by the Zeeman field, but they fluctuate on long timescales.

In a slowly-fluctuating Larmor frequency landscape like that caused by nuclear spins there are two sources of decoherence: shot-to-shot variations in the amount of time the electron spends in each part of the landscape, and long-time fluctuations in the landscape itself. We treated decoherence due shot-to-shot variations in Sec. VI. (There we focused on g -factor variation due to other contributions to disorder in the Larmor frequency, e.g. alloy disorder, but the treatment applies just as well to the nuclear spin contribution.) In this section we treat decoherence due to fluctuations in the nuclear spins themselves; we then briefly return to the nuclear spin contribution to the shot-to-shot variation.

The nuclear spins interact with the electron spin via a contact hyperfine interaction [3, 83]

$$H = \dots + \sum_{\alpha \in \text{impurities}} au \delta(x_e - x_n) \sigma_e \cdot \sigma_n + \dots \quad (40)$$

where x_e, x_n and σ_e, σ_n are electron and nuclear position operators and Pauli matrices, and

$$au = \frac{2}{3} \frac{g\mu_0\mu_B\gamma_n\eta}{wb}, \quad (41)$$

where wb is the cross-sectional area of the dot (cf Table I) and $\eta \sim 100$ is a dimensionless “bunching ratio” [84–88]. (We review the microscopic origin of the effective mass Hamiltonian (40) in App. D.4.) In a dot, this hyperfine interaction leads to Gaussian-in-time dephasing, because the electron is in contact with the same impurities, in the same spin states, for a long time. In an interconnect, by contrast, the electron is in contact with each impurity only briefly, so the dephasing is reduced by motional narrowing. We consider dephasing due to the term

$$aud\delta(x_e - x_n)\sigma_e^z\sigma_n^z. \quad (42)$$

To estimate the magnitude of the dephasing, including motional narrowing, we take the electron to start in a mixture of wavepackets with some characteristic length l_e and consider the effect of a single nuclear spin. The electron state is

$$\rho = \rho_s \otimes \sum_{x,k} p(x)p(k) |\psi(x,k)\rangle\langle\psi(x,k)| \quad (43)$$

where ρ_s is the electron spin state,

$$|\psi_{xk}\rangle = \int dx' e^{-ikx} e^{-(x'-x)^2/4l_e^2} |x'\rangle \quad (44)$$

is a wavepacket with position $\sim x$ and momentum $\sim k$, $p(x)$ is some position distribution, and

$$p(k) \propto e^{-\frac{\hbar^2}{2mk_B T}(k-k_0)^2} \quad (45)$$

is the Gibbs distribution for momentum. Each wavepacket has an interaction matrix element

$$\langle \psi_{xk} | au \delta(x_e - x_\alpha) | \psi_{xk} \rangle \approx \frac{au}{l_e} \quad (46)$$

while the electron is in contact with the impurity.

Ignore, for the moment, momentum relaxation and the electric field. Then an electron in a wavepacket with momentum k is in contact with the impurity for time

$$t_{\text{contact}} \approx l_e/v = l_e m/\hbar k. \quad (47)$$

After averaging over nuclear spin states the electron's spin state evolves by

$$\begin{aligned} \rho_s &\mapsto (1 - \Gamma_k)\rho_s + \Gamma_k \sigma_e^z \rho_s \sigma_e^z, \\ \Gamma_k &\approx \left(\frac{au}{\hbar l_e} t_{\text{contact}} \right)^2 = \left(\frac{mau}{\hbar^2 k} \right)^2. \end{aligned} \quad (48)$$

We give a more careful version of this elementary argument in App. D.1; we derive the same result in scattering theory in App. D.3.

The dephasing probability Γ_k of (48) diverges at small k . The divergence indicates that our perturbative approach breaks down for wavepackets with $k \lesssim mau$, and that—in the absence of momentum relaxation, and ignoring the effects of the electric field—dephasing is dominated by those small- k parts of the momentum distribution. All of this small- k behavior comes about because at small k the electron is slow, so t_{contact} is large.

But this scenario, in which the electron remains in contact with a single impurity for a long time, is not realistic. Because the electron is acted on by the electric field from the resistive topgate and by momentum-relaxation processes, it is best considered as having a random momentum with correlation time τ_k the momentum relaxation time.⁸ For times $t \gg \tau_k \approx 10$ ps, then, the electron has average speed $v_0 = \mu E$, so the contact time is roughly $t_{\text{contact}} \approx l_e/v_0$ and the single-impurity dephasing probability is

$$\Gamma_k \approx (au/\hbar v_0)^2 = \left(\frac{au}{\hbar \mu E} \right)^2 \quad (49)$$

independent of momentum. (We give a somewhat more careful version of this argument in App. D.2, where we assume that the center of each wavepacket undergoes a directed random walk with average speed $v_0 = \mu E$.) Because the dephasing probability is momentum-independent, the integration over the momentum degree of freedom k in the initial state (43) is trivial, and the integration over the position degree of freedom x in (43) is trivial because every wavepacket eventually encounters the impurity. The dephasing due to this single impurity is therefore

$$\Gamma_{\text{single}} = \left(\frac{au}{\hbar \mu E} \right)^2. \quad (50)$$

The dephasing length is given by the linear density of impurities $\lambda = \nu w b$, ν the volumetric density:

$$\frac{1}{L_2} = \Gamma_{\text{single}} \lambda = \left(\frac{2}{3} \frac{g \mu_0 \mu_B \gamma_n \eta}{\hbar \mu E} \right)^2 \frac{\nu}{w b}. \quad (51)$$

At 800 ppm, $\nu \approx 0.04 \text{ nm}^{-3}$ for

$$\frac{1}{L_2} \approx (1.4 \times 10^5 \text{ m})^{-1}. \quad (52)$$

In App. D.5 we use the results of App. B to compute the effect of variation in how long the electron spends near each spin—that is, the disorder average of the shot-to-shot variance, as opposed to the shot-to-shot average of the disorder variance. We find

$$\frac{1}{L_2} \approx \left(\frac{2\mu_0}{3} \frac{g \mu_B \gamma_n \eta}{\hbar \mu E} \right)^2 \frac{\nu}{w b} \frac{k_B T}{e E l_e}; \quad (53)$$

For our parameters and $l_e = 100$ nm, this differs from (51) by $T/eEl_e \approx 0.26$, so (51) provides an adequate estimate of the effect of nuclear spins.

The dependence $\Gamma \propto (wb)^{-1}$, wb the cross-sectional area of the channel, deserves comment. This comes about because the hyperfine coupling is $au \propto |\psi(\mathbf{r}_j)|^2 \propto (wb)^{-1}$, $\psi(\mathbf{r}_j)$ the electron wavefunction at the impurity, and the hyperfine coupling enters the dephasing probability as $(au)^2 \propto (wb)^{-2}$. As the channel grows wider, that drop in the hyperfine coupling outweighs the increase in the number of impurities the electron contacts.

VIII. CONCLUSION

We proposed to use a resistive topgate to connect quantum dots in silicon heterostructures. When the topgate is biased it creates a 1D channel between the dots; when a current runs through the topgate, the concomitant electric field drives the electron from source dot to target dot. We considered dephasing and relaxation of the electron's spin state due to spin-orbit coupling, valley effects, and nuclear spin impurities. We found that both dephasing and relaxation are dominated by spin-orbit coupling, via

⁸ Note that in Drudé theory the momentum relaxation time is also the time it takes for the electric field to accelerate the electron from a standing start to the steady-state velocity.

the D'yakonov-Perel' effect, leading to characteristic relaxation and dephasing lengths $L_1 \approx 0.74$ m, $L_2 \approx 15$ mm .

We have focused on transport, not on the one-time dot entry and exit processes. Tunneling to and from the dot will likely be at least somewhat spin-selective, due to magnetic field gradients or g -factor variation. In principle this spin-selective tunneling gives an artificial spin-orbit coupling that couples the spin state to charge noise. In practice we do not expect this effect to be larger for our devices than for coherent tunneling between dots, which has been demonstrated with high fidelity [21–30].

We assume that electron transport is controlled by incoherent, inelastic scattering. Inelastic scattering is crucial: the electron moves in a potential landscape created by the resistive topgate, from high potential energy to low potential energy, and that energy must be dissipated by inelastic scattering processes. We expect that phonon emission, together with scattering between the electron in the channel and the many conduction electrons in the topgate, provides the necessary dissipation. We further assume that this scattering can be treated in a Drudé-like picture, implicitly resting on a Boltzmann equation for populations in momentum states.

If transport is controlled instead by static disorder, e.g. the Coulomb disorder treated by [56], our Drudé-like picture is not appropriate. In this case a better picture starts with localized eigenstates, and considers Mott variable-range hopping between those eigenstates. The spin-orbit calculations of Sec. IV no longer apply; our valley-diabaticity assumptions of Sec. V have to be reexamined; and nuclear spin impurities become more important, because the electron spends more time in contact with each spin and the motional narrowing of Sec. VII becomes less effective. Experiments are ultimately needed to determine which regime the device is in.

One may be able to escape this disorder-controlled regime by adding electrons to the channel, which would fill tightly localized low energy bound states. In this scenario the electron would travel through weakly-localized high-energy states above a Fermi level. The crossover would be broadly similar to the percolation threshold in 2D materials, though instead of a percolation transition one would hope merely to weaken the effect of disorder relative to other (inelastic) scattering sources. Adding electrons to the channel in this way would, however, introduce other sources of decoherence.

The resistive interconnect we propose imposes certain design tradeoffs. The interconnect's relaxation and decoherence lengths are controlled by the spin orbit coupling

coefficients; any increase beyond the ~ 1 peV · cm expected for Si/SiGe wells threatens interconnect fidelities. So resistive interconnects will require substantial effort in a “wobble well”, in which oscillating Ge concentrations in the Si well are used to control valley splitting and increase spin-orbit coupling [55, 89–91]. Resistive interconnects likewise may require more effort in SiMOS or Ge hole devices, where spin-orbit coupling coefficients are larger than the Si/Si_xGe_{1-x} devices we consider [92, 93]. In such systems it may be better to use conveyor-mode shuttling: in conveyor-mode shuttling the electron's position state is coherent, so large spin-orbit coupling protects the electron spin [60].

A functioning resistive interconnect will create a number of new architectural possibilities, all requiring further theory work. In the near term, we look forward to using the resistive topgate for measurement in a solid state Stern Gerlach experiment [94, 95]. If the topgates form a Y near a micromagnet, the micromagnet will produce a magnetic field gradient that will divide spin-up and spin-down electrons between the arms of the Y. Designing such a device will benefit from theoretical modeling to set the device parameters—the micromagnet strength, the electron speed, the width of the channel at the Y, etc.—to maximize the measurement fidelity.

In the longer term, high-fidelity interconnects will enable the genuinely long-range gates required by many error correcting codes. Our calculations suggest that a resistive interconnect can transport spin states with fidelities $\gtrsim 99.9\%$ over distances of 10-100 μ m, depending on spin-orbit coupling and temperature. If a single qubit in a grid requires 500 nm, this is a range of 20-200 qubits. But designing a good interconnect architecture for a many-qubit device will require answering many related theory questions, from high-level questions about e.g. routing protocols to low-level device physics questions about e.g. the behavior of the electrons at corners.

ACKNOWLEDGMENTS

We thank Ben Woods, Merritt Losert, Steve Lyon, Ryan Jock, Jan Krzywda, Mike Winer, Yuxin Wang, Jay Deep Sau, and Katharina Laubscher for helpful discussions. This work was supported in part by ARO grant W911NF-23-1-0242, ARO grant W911NF-23-1-0258, and NSF QLCI grant OMA-2120757. CDW also acknowledges DOE-ASCR Quantum Computing Application Teams program for support under fieldwork proposal number ERKJ347.

-
- [1] D. Loss and D. P. DiVincenzo, Quantum computation with quantum dots, *Physical Review A* **57**, 120 (1998), publisher: American Physical Society.
 [2] F. A. Zwanenburg, A. S. Dzurak, A. Morello, M. Y. Simmons, L. C. L. Hollenberg, G. Klimeck, S. Rogge, S. N.

- Coppersmith, and M. A. Eriksson, Silicon quantum electronics, *Reviews of Modern Physics* **85**, 961 (2013), publisher: American Physical Society.
 [3] G. Burkard, T. D. Ladd, A. Pan, J. M. Nichol, and J. R. Petta, Semiconductor spin qubits, *Reviews of Modern*

- Physics **95**, 025003 (2023), publisher: American Physical Society.
- [4] J. Yoneda, K. Takeda, T. Otsuka, T. Nakajima, M. R. Delbecq, G. Allison, T. Honda, T. Kodera, S. Oda, Y. Hoshi, N. Usami, K. M. Itoh, and S. Tarucha, A quantum-dot spin qubit with coherence limited by charge noise and fidelity higher than 99.9%, *Nature Nanotechnology* **13**, 102 (2018), number: 2 Publisher: Nature Publishing Group.
 - [5] X. Xue, M. Russ, N. Samkharadze, B. Undseth, A. Sammak, G. Scappucci, and L. M. K. Vandersypen, Quantum logic with spin qubits crossing the surface code threshold, *Nature* **601**, 343 (2022), number: 7893 Publisher: Nature Publishing Group.
 - [6] A. Noiri, K. Takeda, T. Nakajima, T. Kobayashi, A. Sammak, G. Scappucci, and S. Tarucha, Fast universal quantum gate above the fault-tolerance threshold in silicon, *Nature* **601**, 338 (2022), number: 7893 Publisher: Nature Publishing Group.
 - [7] A. R. Mills, C. R. Guinn, M. M. Feldman, A. J. Sigillito, M. J. Gullans, M. Rakher, J. Kerckhoff, C. A. C. Jackson, and J. R. Petta, High fidelity state preparation, quantum control, and readout of an isotopically enriched silicon spin qubit (2022), arXiv:2204.09551 [cond-mat, physics:quant-ph].
 - [8] A. R. Mills, C. R. Guinn, M. J. Gullans, A. J. Sigillito, M. M. Feldman, E. Nielsen, and J. R. Petta, Two-qubit silicon quantum processor with operation fidelity exceeding 99%, *Science Advances* **8**, eabn5130 (2022), publisher: American Association for the Advancement of Science.
 - [9] N. M. Linke, D. Maslov, M. Roetteler, S. Debnath, C. Figgatt, K. A. Landsman, K. Wright, and C. Monroe, Experimental Comparison of Two Quantum Computing Architectures, *Proceedings of the National Academy of Sciences* **114**, 3305 (2017), arXiv:1702.01852 [quant-ph].
 - [10] N. P. Breuckmann and J. N. Eberhardt, Quantum Low-Density Parity-Check Codes, *PRX Quantum* **2**, 040101 (2021), arXiv:2103.06309 [quant-ph].
 - [11] J. M. Taylor, H.-A. Engel, W. Dür, A. Yacoby, C. M. Marcus, P. Zoller, and M. D. Lukin, Fault-tolerant architecture for quantum computation using electrically controlled semiconductor spins, *Nature Physics* **1**, 177 (2005).
 - [12] L. M. K. Vandersypen, H. Bluhm, J. S. Clarke, A. S. Dzurak, R. Ishihara, A. Morello, D. J. Reilly, L. R. Schreiber, and M. Veldhorst, Interfacing spin qubits in quantum dots and donors—hot, dense, and coherent, *npj Quantum Information* **3**, 1 (2017), number: 1 Publisher: Nature Publishing Group.
 - [13] A. D. Greentree, J. H. Cole, A. R. Hamilton, and L. C. L. Hollenberg, Coherent electronic transfer in quantum dot systems using adiabatic passage, *Physical Review B* **70**, 235317 (2004).
 - [14] A. D. Greentree, S. J. Devitt, and L. C. L. Hollenberg, Quantum-information transport to multiple receivers, *Physical Review A* **73**, 032319 (2006).
 - [15] M. Busl, G. Granger, L. Gaudreau, R. Sánchez, A. Kam, M. Pioro-Ladrière, S. A. Studenikin, P. Zawadzki, Z. R. Wasilewski, A. S. Sachrajda, and G. Platero, Bipolar spin blockade and coherent state superpositions in a triple quantum dot, *Nature Nanotechnology* **8**, 261 (2013).
 - [16] R. Sánchez, G. Granger, L. Gaudreau, A. Kam, M. Pioro-Ladrière, S. A. Studenikin, P. Zawadzki, A. S. Sachrajda, and G. Platero, Long-Range Spin Transfer in Triple Quantum Dots, *Physical Review Letters* **112**, 176803 (2014).
 - [17] Y. Ban, X. Chen, S. Kohler, and G. Platero, Spin Entangled State Transfer in Quantum Dot Arrays: Coherent Adiabatic and Speed-Up Protocols, *Advanced Quantum Technologies* **2**, 1900048 (2019).
 - [18] K. Groenland, C. Groenland, and R. Kramer, Stimulated Raman adiabatic passage-like protocols for amplitude transfer generalize to many bipartite graphs, *Journal of Mathematical Physics* **61**, 072201 (2020).
 - [19] D. Stefanatos and E. Paspalakis, Speeding up adiabatic passage with an optimal modified Roland–Cerf protocol, *Journal of Physics A: Mathematical and Theoretical* **53**, 115304 (2020).
 - [20] M. J. Gullans and J. R. Petta, Coherent transport of spin by adiabatic passage in quantum dot arrays, *Physical Review B* **102**, 155404 (2020).
 - [21] T. A. Baart, M. Shafiei, T. Fujita, C. Reichl, W. Wegscheider, and L. M. K. Vandersypen, Single-spin CCD, *Nature Nanotechnology* **11**, 330 (2016).
 - [22] H. Flentje, P.-A. Mortemousque, R. Thalineau, A. Ludwig, A. D. Wieck, C. Bäuerle, and T. Meunier, Coherent long-distance displacement of individual electron spins, *Nature Communications* **8**, 501 (2017).
 - [23] T. Fujita, T. A. Baart, C. Reichl, W. Wegscheider, and L. M. K. Vandersypen, Coherent shuttle of electron-spin states, *npj Quantum Information* **3**, 1 (2017).
 - [24] A. R. Mills, D. M. Zajac, M. J. Gullans, F. J. Schupp, T. M. Hazard, and J. R. Petta, Shuttling a single charge across a one-dimensional array of silicon quantum dots, *Nature Communications* **10**, 1063 (2019).
 - [25] P.-A. Mortemousque, B. Jadot, E. Chanrion, V. Thiney, C. Bäuerle, A. Ludwig, A. D. Wieck, M. Urdampilleta, and T. Meunier, Enhanced Spin Coherence while Displacing Electron in a Two-Dimensional Array of Quantum Dots, *PRX Quantum* **2**, 030331 (2021).
 - [26] J. Yoneda, W. Huang, M. Feng, C. H. Yang, K. W. Chan, T. Tantau, W. Gilbert, R. C. C. Leon, F. E. Hudson, K. M. Itoh, A. Morello, S. D. Bartlett, A. Laucht, A. Saraiva, and A. S. Dzurak, Coherent spin qubit transport in silicon, *Nature Communications* **12**, 4114 (2021).
 - [27] A. Noiri, K. Takeda, T. Nakajima, T. Kobayashi, A. Sammak, G. Scappucci, and S. Tarucha, A shuttling-based two-qubit logic gate for linking distant silicon quantum processors, *Nature Communications* **13**, 5740 (2022).
 - [28] A. Zwerver, S. Amitonov, S. de Snoo, M. Madzik, M. Rimbach-Russ, A. Sammak, G. Scappucci, and L. Vandersypen, Shuttling an Electron Spin through a Silicon Quantum Dot Array, *PRX Quantum* **4**, 030303 (2023).
 - [29] F. van Riggelen-Doelman, C.-A. Wang, S. L. de Snoo, W. I. L. Lawrie, N. W. Hendrickx, M. Rimbach-Russ, A. Sammak, G. Scappucci, C. Déprez, and M. Veldhorst, Coherent spin qubit shuttling through germanium quantum dots (2023), arxiv:2308.02406 [cond-mat, physics:quant-ph].
 - [30] M. D. Smet, Y. Matsumoto, A.-M. J. Zwerver, L. Trypuzen, S. L. de Snoo, S. V. Amitonov, A. Sammak, N. Samkharadze, O. Gül, R. N. M. Wasserman, M. Rimbach-Russ, G. Scappucci, and L. M. K. Vandersypen, High-fidelity single-spin shuttling in silicon

- (2024), arXiv:2406.07267.
- [31] V. Langrock, J. A. Krzywdka, N. Focke, I. Seidler, L. R. Schreiber, and L. Cywiński, Blueprint of a Scalable Spin Qubit Shuttle Device for Coherent Mid-Range Qubit Transfer in Disordered Si/SiGe/SiO_2 , PRX Quantum **4**, 020305 (2023).
- [32] I. Seidler, T. Struck, R. Xue, N. Focke, S. Trellenkamp, H. Bluhm, and L. R. Schreiber, Conveyor-mode single-electron shuttling in Si/SiGe for a scalable quantum computing architecture, npj Quantum Information **8**, 1 (2022).
- [33] T. Struck, M. Volmer, L. Visser, T. Offermann, R. Xue, J.-S. Tu, S. Trellenkamp, L. Cywiński, H. Bluhm, and L. R. Schreiber, Spin-EPR-pair separation by conveyor-mode single electron shuttling in Si/SiGe (2023), arxiv:2307.04897 [cond-mat, physics:quant-ph].
- [34] R. Xue, M. Beer, I. Seidler, S. Humpohl, J.-S. Tu, S. Trellenkamp, T. Struck, H. Bluhm, and L. R. Schreiber, Si/SiGe QuBus for single electron information-processing devices with memory and micron-scale connectivity function (2023), arxiv:2306.16375 [cond-mat, physics:quant-ph].
- [35] L. Childress, A. S. Sørensen, and M. D. Lukin, Mesoscopic cavity quantum electrodynamics with quantum dots, Physical Review A **69**, 042302 (2004).
- [36] J. Majer, J. M. Chow, J. M. Gambetta, J. Koch, B. R. Johnson, J. A. Schreier, L. Frunzio, D. I. Schuster, A. A. Houck, A. Wallraff, A. Blais, M. H. Devoret, S. M. Girvin, and R. J. Schoelkopf, Coupling superconducting qubits via a cavity bus, Nature **449**, 443 (2007).
- [37] J. J. Viennot, M. C. Dartiailh, A. Cottet, and T. Kontos, Coherent coupling of a single spin to microwave cavity photons, Science **349**, 408 (2015).
- [38] X. Mi, M. Benito, S. Putz, D. M. Zajac, J. M. Taylor, G. Burkard, and J. R. Petta, A coherent spin-photon interface in silicon, Nature **555**, 599 (2018).
- [39] N. Samkharadze, G. Zheng, N. Kalhor, D. Brousse, A. Sammak, U. C. Mendes, A. Blais, G. Scappucci, and L. M. K. Vandersypen, Strong spin-photon coupling in silicon, Science **359**, 1123 (2018).
- [40] A. J. Landig, J. V. Koski, P. Scarlino, U. C. Mendes, A. Blais, C. Reichl, W. Wegscheider, A. Wallraff, K. Ensslin, and T. Ihn, Coherent spin-photon coupling using a resonant exchange qubit, Nature **560**, 179 (2018).
- [41] F. Borjans, X. G. Croot, X. Mi, M. J. Gullans, and J. R. Petta, Resonant microwave-mediated interactions between distant electron spins, Nature **577**, 195 (2020).
- [42] P. Harvey-Collard, J. Dijkema, G. Zheng, A. Sammak, G. Scappucci, and L. M. K. Vandersypen, Coherent Spin-Spin Coupling Mediated by Virtual Microwave Photons, Physical Review X **12**, 021026 (2022).
- [43] J. Dijkema, X. Xue, P. Harvey-Collard, M. Rimbach-Russ, S. L. de Snoo, G. Zheng, A. Sammak, G. Scappucci, and L. M. K. Vandersypen, Two-qubit logic between distant spins in silicon (2023), arxiv:2310.16805 [cond-mat, physics:quant-ph].
- [44] J. M. Shilton, V. I. Talyanskii, M. Pepper, D. A. Ritchie, J. E. F. Frost, C. J. B. Ford, C. G. Smith, and G. A. C. Jones, High-frequency single-electron transport in a quasi-one-dimensional GaAs channel induced by surface acoustic waves, Journal of Physics: Condensed Matter **8**, L531 (1996).
- [45] B. Jadot, P.-A. Mortemousque, E. Chanrion, V. Thiney, A. Ludwig, A. D. Wieck, M. Urdampilleta, C. Bäuerle, and T. Meunier, Distant spin entanglement via fast and coherent electron shuttling, Nature Nanotechnology **16**, 570 (2021), arxiv:2004.02727 [cond-mat].
- [46] C. J. van Diepen, T.-K. Hsiao, U. Mukhopadhyay, C. Reichl, W. Wegscheider, and L. M. K. Vandersypen, Electron cascade for spin readout, Nature Communications **12**, 77 (2021), arxiv:2002.08925 [cond-mat, physics:quant-ph].
- [47] B. Hetényi, A. Mook, J. Klinovaja, and D. Loss, Long-distance coupling of spin qubits via topological magnons, Physical Review B **106**, 235409 (2022).
- [48] X. Mi, T. M. Hazard, C. Payette, K. Wang, D. M. Zajac, J. V. Cady, and J. R. Petta, Magnetotransport studies of mobility limiting mechanisms in undoped Si/SiGe heterostructures, Physical Review B **92**, 035304 (2015).
- [49] V. I. Perel' and D'yakonov, Spin orientation of electrons associated with the interband absorption of light in semiconductors, Soviet Physics JETP **33**, 1053 (1971).
- [50] D'yakonov, M.I., Spin relaxation of conduction electrons in noncentrosymmetric semiconductors, Soviet Physics Solid State **13**, 3023 (1972).
- [51] G.E. Pikus and A.N. Titkanov, Spin Relaxation under Optical Orientation in Semiconductors, in *Optical Orientation, Modern Problems in Condensed Matter Sciences*, Vol. 8, edited by F. Meier and B.P. Zakharchenya (North-Holland Physics Publishing, Amsterdam, 1984) pp. 73–131.
- [52] Z. Wilamowski, W. Jantsch, N. Sandersfeld, M. Mühlberger, F. Schäffler, and S. Lyon, Spin relaxation and g-factor of two-dimensional electrons in Si/SiGe quantum wells, Physica E: Low-dimensional Systems and Nanostructures **16**, 111 (2003).
- [53] M. O. Nestoklon, E. L. Ivchenko, J.-M. Jancu, and P. Voisin, Electric field effect on electron spin splitting in Si/Ge/Si quantum wells, Physical Review B **77**, 155328 (2008).
- [54] R. Ferdous, E. Kawakami, P. Scarlino, M. P. Nowak, D. R. Ward, D. E. Savage, M. G. Lagally, S. N. Coppersmith, M. Friesen, M. A. Eriksson, L. M. K. Vandersypen, and R. Rahman, Valley dependent anisotropic spin splitting in silicon quantum dots, npj Quantum Information **4**, 26 (2018).
- [55] M. P. Losert, M. A. Eriksson, R. Joynt, R. Rahman, G. Scappucci, S. N. Coppersmith, and M. Friesen, Practical Strategies for Enhancing the Valley Splitting in Si/SiGe Quantum Wells (2023).
- [56] Y. Huang and S. D. Sarma, Understanding disorder in Silicon quantum computing platforms: Scattering mechanisms in Si/SiGe quantum wells (2023), arXiv:2312.07717 [cond-mat].
- [57] P. W. Anderson, Absence of Diffusion in Certain Random Lattices, Physical Review **109**, 1492 (1958).
- [58] N. F. Mott, Conduction in non-crystalline systems: I. localized electronic states in disordered systems, The Philosophical Magazine: A Journal of Theoretical Experimental and Applied Physics **17**, 1259 (1968), publisher: Taylor & Francis eprint: <https://doi.org/10.1080/14786436808223200>.
- [59] P. A. Lee and T. V. Ramakrishnan, Disordered electronic systems, Reviews of Modern Physics **57**, 287 (1985).
- [60] S. Bosco, J. Zou, and D. Loss, High-fidelity spin qubit shuttling via large spin-orbit interaction, PRX Quantum **5**, 020353 (2024), arXiv:2311.15970 [cond-mat,

- physics:quant-ph].
- [61] P. W. Deelman, L. F. Edge, and C. A. Jackson, Metamorphic materials for quantum computing, *MRS Bulletin* **41**, 224 (2016).
- [62] B. Schumacher, Sending quantum entanglement through noisy channels (1996), arXiv:quant-ph/9604023.
- [63] M. A. Nielsen, The entanglement fidelity and quantum error correction, arXiv:quant-ph/9606012 (1996), arXiv: quant-ph/9606012.
- [64] A. A. Mele, Introduction to Haar Measure Tools in Quantum Information: A Beginner's Tutorial, *Quantum* **8**, 1340 (2024), arXiv:2307.08956 [quant-ph].
- [65] R. Kubo, Statistical-Mechanical Theory of Irreversible Processes. I, *Journal of the Physical Society of Japan* **12**, 570 (1957).
- [66] P. C. Martin and J. Schwinger, Theory of Many-Particle Systems. I, *Physical Review* **115**, 1342 (1959).
- [67] R. Haag, N. M. Hugenholtz, and M. Winnink, On the equilibrium states in quantum statistical mechanics, *Communications in Mathematical Physics* **5**, 215 (1967).
- [68] M. P. Losert, M. Oberländer, J. D. Teske, M. Volmer, L. R. Schreiber, H. Bluhm, S. N. Coppersmith, and M. Friesen, Strategies for enhancing spin-shuttling fidelities in Si/SiGe quantum wells with random-alloy disorder (2024), arXiv:2405.01832 [cond-mat].
- [69] C. H. Yang, A. Rossi, R. Ruskov, N. S. Lai, F. A. Mohiyaddin, S. Lee, C. Tahan, G. Klimeck, A. Morello, and A. S. Dzurak, Spin-valley lifetimes in a silicon quantum dot with tunable valley splitting, *Nature Communications* **4**, 2069 (2013), publisher: Nature Publishing Group.
- [70] P. Huang and X. Hu, Spin relaxation in a Si quantum dot due to spin-valley mixing, *Physical Review B* **90**, 235315 (2014), publisher: American Physical Society.
- [71] C. Tahan and R. Joynt, Relaxation of excited spin, orbital, and valley qubit states in ideal silicon quantum dots, *Physical Review B* **89**, 075302 (2014), publisher: American Physical Society.
- [72] X. Hao, R. Ruskov, M. Xiao, C. Tahan, and H. Jiang, Electron spin resonance and spin-valley physics in a silicon double quantum dot, *Nature Communications* **5**, 3860 (2014), publisher: Nature Publishing Group.
- [73] A. Corna, L. Bourdet, R. Maurand, A. Crippa, D. Kotekar-Patil, H. Bohuslavskyi, R. Laviéville, L. Hutin, S. Barraud, X. Jehl, M. Vinet, S. De Franceschi, Y.-M. Niquet, and M. Sanquer, Electrically driven electron spin resonance mediated by spin-valley-orbit coupling in a silicon quantum dot, *npj Quantum Information* **4**, 1 (2018), number: 1 Publisher: Nature Publishing Group.
- [74] A. Hollmann, T. Struck, V. Langrock, A. Schmidbauer, F. Schauer, T. Leonhardt, K. Sawano, H. Riemann, N. V. Abrosimov, D. Bougeard, and L. R. Schreiber, Large, Tunable Valley Splitting and Single-Spin Relaxation Mechanisms in a Si/Si_xGe_{1-x} Quantum Dot, *Physical Review Applied* **13**, 034068 (2020), publisher: American Physical Society.
- [75] N. E. Penthorn, J. S. Schoenfeld, L. F. Edge, and H. Jiang, Direct Measurement of Electron Intervalley Relaxation in a si/sige Quantum Dot, *Physical Review Applied* **14**, 054015 (2020), publisher: American Physical Society.
- [76] X. Zhang, R.-Z. Hu, H.-O. Li, F.-M. Jing, Y. Zhou, R.-L. Ma, M. Ni, G. Luo, G. Cao, G.-L. Wang, X. Hu, H.-W. Jiang, G.-C. Guo, and G.-P. Guo, Giant Anisotropy of Spin Relaxation and Spin-Valley Mixing in a Silicon Quantum Dot, *Physical Review Letters* **124**, 257701 (2020), publisher: American Physical Society.
- [77] A. Hosseinkhani and G. Burkard, Relaxation of single-electron spin qubits in silicon in the presence of interface steps, *Physical Review B* **104**, 085309 (2021), publisher: American Physical Society.
- [78] R. M. Jock, N. T. Jacobson, M. Rudolph, D. R. Ward, M. S. Carroll, and D. R. Luhman, A silicon singlet-triplet qubit driven by spin-valley coupling, *Nature Communications* **13**, 641 (2022).
- [79] M. Volmer, T. Struck, A. Sala, B. Chen, M. Oberländer, T. Offermann, R. Xue, L. Visser, J.-S. Tu, S. Trellenkamp, L. Cywiński, H. Bluhm, and L. R. Schreiber, Mapping of valley-splitting by conveyor-mode spin-coherent electron shuttling (2023), arxiv:2312.17694 [cond-mat, physics:quant-ph].
- [80] X. Cai, E. J. Connors, L. F. Edge, and J. M. Nichol, Coherent spin-valley oscillations in silicon, *Nature Physics* **19**, 386 (2023).
- [81] R. M. Jock, N. T. Jacobson, P. Harvey-Collard, A. M. Mounce, V. Srinivasa, D. R. Ward, J. Anderson, R. Manginell, J. R. Wendt, M. Rudolph, T. Pluym, J. K. Gamble, A. D. Baczewski, W. M. Witzel, and M. S. Carroll, A silicon metal-oxide-semiconductor electron spin-orbit qubit, *Nature Communications* **9**, 1768 (2018), number: 1 Publisher: Nature Publishing Group.
- [82] B. M. Maune, M. G. Borselli, B. Huang, T. D. Ladd, P. W. Deelman, K. S. Holabird, A. A. Kiselev, I. Alvarado-Rodriguez, R. S. Ross, A. E. Schmitz, M. Sokolich, C. A. Watson, M. F. Gyure, and A. T. Hunter, Coherent singlet-triplet oscillations in a silicon-based double quantum dot, *Nature* **481**, 344 (2012), publisher: Nature Publishing Group.
- [83] G. Feher, Electron Spin Resonance Experiments on Donors in Silicon. I. Electronic Structure of Donors by the Electron Nuclear Double Resonance Technique, *Physical Review* **114**, 1219 (1959).
- [84] R. G. Shulman and B. J. Wyluda, Nuclear Magnetic Resonance of Si 29 in n - and p -Type Silicon, *Physical Review* **103**, 1127 (1956).
- [85] D. K. Wilson, Electron Spin Resonance Experiments on Shallow Donors in Germanium, *Physical Review* **134**, A265 (1964).
- [86] R. K. Sundfors and D. F. Holcomb, Nuclear Magnetic Resonance Studies of the Metallic Transition in Doped Silicon, *Physical Review* **136**, A810 (1964).
- [87] L. V. C. Assali, H. M. Petrilli, R. B. Capaz, B. Koiller, X. Hu, and S. Das Sarma, Hyperfine interactions in silicon quantum dots, *Physical Review B* **83**, 165301 (2011).
- [88] P. Philippopoulos, S. Chesi, and W. A. Coish, First-principles hyperfine tensors for electrons and holes in GaAs and silicon, *Physical Review B* **101**, 115302 (2020).
- [89] T. McJunkin, B. Harpt, Y. Feng, M. P. Losert, R. Rahman, J. P. Dodson, M. A. Wolfe, D. E. Savage, M. G. Lagally, S. N. Coppersmith, M. Friesen, R. Joynt, and M. A. Eriksson, SiGe quantum wells with oscillating Ge concentrations for quantum dot qubits, *Nature Communications* **13**, 7777 (2022), number: 1 Publisher: Nature

Publishing Group.

- [90] Y. Feng and R. Joynt, Enhanced valley splitting in Si layers with oscillatory Ge concentration, *Physical Review B* **106**, 085304 (2022), publisher: American Physical Society.
- [91] B. D. Woods, M. A. Eriksson, R. Joynt, and M. Friesen, Spin-orbit enhancement in Si/SiGe heterostructures with oscillating Ge concentration, *Physical Review B* **107**, 035418 (2023), arXiv:2210.01700 [cond-mat].
- [92] R. Ruskov, M. Veldhorst, A. S. Dzurak, and C. Tahan, Electron g -factor of valley states in realistic silicon quantum dots, *Physical Review B* **98**, 245424 (2018), arXiv:1708.04555 [cond-mat].
- [93] C. Adelsberger, S. Bosco, J. Klinovaja, and D. Loss, Enhanced orbital magnetic field effects in Ge hole nanowires, *Physical Review B* **106**, 235408 (2022), publisher: American Physical Society.
- [94] C. H. W. Barnes, J. M. Shilton, and A. M. Robinson, Quantum computation using electrons trapped by surface acoustic waves, *Physical Review B* **62**, 8410 (2000), publisher: American Physical Society.
- [95] J. Wróbel, Stern-Gerlach effect and spin filtering in the solid state, *physica status solidi c* **3**, 4214 (2006), eprint: <https://onlinelibrary.wiley.com/doi/pdf/10.1002/pssc.200672886>.
- [96] M. Prada, G. Klimeck, and R. Joynt, Spin-orbit splittings in Si/SiGe quantum wells: from ideal Si membranes to realistic heterostructures, *New Journal of Physics* **13**, 013009 (2011).
- [97] Z. Wilamowski, N. Sandersfeld, W. Jantsch, D. Többen, and F. Schäffler, Screening Breakdown on the Route toward the Metal-Insulator Transition in Modulation Doped Si/SiGe Quantum Wells, *Physical Review Letters* **87**, 026401 (2001), publisher: American Physical Society.
- [98] H.-P. Breuer and F. Petruccione, *The theory of open quantum systems* (Oxford University Press, Oxford, 2002) section: xxi, 625 pages : illustrations ; 25 cm.
- [99] R. J. Schoelkopf, A. A. Clerk, S. M. Girvin, K. W. Lehnert, and M. H. Devoret, Qubits as Spectrometers of Quantum Noise, in *Quantum Noise in Mesoscopic Physics*, edited by Y. V. Nazarov (Springer Netherlands, Dordrecht, 2003) pp. 175–203.
- [100] E. B. Hale and R. L. Mieher, Shallow Donor Electrons in Silicon. I. Hyperfine Interactions from ENDOR Measurements, *Physical Review* **184**, 739 (1969).
- [101] J. M. Luttinger and W. Kohn, Hyperfine Splitting of Donor States in Silicon, *Physical Review* **96**, 802 (1954).
- [102] W. Kohn and J. M. Luttinger, Theory of Donor Levels in Silicon, *Physical Review* **97**, 1721 (1955).

Appendix A: Spin-orbit coupling

In these appendices we take $\hbar = k_B = 1$, except where noted.

A.1. Value of the spin-orbit coupling coefficient

The values of the spin-orbit coupling coefficients α, β (for Rashba SOC $H_R = \alpha(\sigma^x k_y - \sigma^y k_x)$ and Dresselhaus-like $H_D = \beta(\sigma^x k_x - \sigma^y k_y)$) depend on many device details, including the electric field, the quantum well thickness, and the interface disorder [96]. In our model device we take the Rashba and Dresselhaus spin orbit coupling to have values $\alpha = 0.2 \text{peV} \cdot \text{cm}$ and $\beta = 1 \text{peV} \cdot \text{cm}$ respectively. This is motivated by conduction electron experiments in Si/SiGe quantum wells at finite electron density [52] g -factor anisotropy experiments in Si/SiGe quantum dots [54], and tight binding calculations [53, 91, 96]

Wilamowski et al. [52] report conduction-electron spin resonance (CESR) and spin echo experiments. (Their device is described in [97].) They apply an external magnetic field at a variable angle to the quantum well; they find that the dependence of the g -factor and the electron T_1 and T_2 on the magnetic field angle and the filling can all be explained with a single fit parameter, a Rashba spin-orbit coupling coefficient

$$\alpha = 0.55 \text{ peV} \cdot \text{cm} . \quad (\text{A1})$$

They do not consider whether their data can fit by a Dresselhaus spin-orbit coupling. Later numerical work [53, 91, 96] finds that these heterostructures are likely to display larger Dresselhaus than Rashba spin-orbit coupling (vide infra).

Ferdous et al. [54] measure the g -factor anisotropy in a SiGe/Si/SiGe quantum dot, and back out a Dresselhaus spin-orbit coupling via effective mass theory (and comparisons to atomistic tight-binding models). They find Dresselhaus spin-orbit coupling

$$\beta \approx 1 \text{ peV} \cdot \text{cm} \quad (\text{A2})$$

with opposite signs in the dot's two valley states. They do not quote a Rashba spin-orbit coupling.

Tight-binding calculations [53] find⁹

$$\begin{aligned} \alpha &\sim 0.2 \text{ peV} \cdot \text{cm} \\ \beta &\sim 3.5 \text{ peV} \cdot \text{cm} . \end{aligned} \quad (\text{A3})$$

at a transverse electric field $5 \cdot 10^6 \text{V/m}$, for a narrow well of 31 monoatomic plains [53, Fig. 3] The couplings decrease as the well thickness increases; for a larger 20 nm well, [91, Fig. 3] find¹⁰

$$\begin{aligned} \alpha &\sim 0.2 \text{ peV} \cdot \text{cm} \\ \beta &\sim 1 \text{ peV} \cdot \text{cm} . \end{aligned} \quad (\text{A4})$$

⁹ Note that [53] reverses the notation: they write α for Dresselhaus and β for Rashba.

¹⁰ [91] goes on to consider so-called “wiggle wells”, with an oscillating germanium concentration in the well; these wiggle wells have higher spin-orbit coupling.

For wells with clean interfaces the zero-electric-field couplings depend strongly on the number of monolayers in the well, for symmetry reasons (see [53] for a concise discussion, or [96] for a more pedagogical discussion). Real wells suffer alloy disorder, which smooths the dependence on the number of monolayers [96].

A.2. Lindblad dynamics

In general consider

$$H = H_A + H_B + AB, \quad (\text{A5})$$

where H_A and H_B act on a system of interest and a bath, respectively, and in the small coupling AB A acts on system and B on bath. Go to the interaction picture with respect to H_A and H_B , treat the coupling perturbatively, and make some standard approximations (Born-Markov and rotating wave). Then the dynamics of the density matrix for the system of interest is [98][3.3.1] (cf [99])

$$\frac{d}{dt}\rho = \sum_{\omega=0,\pm\Omega} S_B(\omega) \left[A(\omega)\rho A^\dagger(\omega) - \frac{1}{2} \{A^\dagger(\omega A(\omega), \rho)\} \right], \quad (\text{A6})$$

where the Lindblad operators are the frequency components of A in an H_A eigenbasis

$$A(\omega) = \sum_{E_{j'} - E_j = \omega} |j'\rangle\langle j'| A |j\rangle\langle j| \quad (\text{A7})$$

and the rates are given by the B correlation function

$$S_B(\omega) = \text{Tr } B(t)B(0)e^{-\beta H_B}. \quad (\text{A8})$$

Given the approximations that lead to the master equation, this correlation function is the only property of the bath that enters.

In our case the electron spin is the system of interest, and the momentum together with all the scattering sources—impurities, phonons, conduction electrons, etc.—form the bath. Since k_0 is a scalar, the system Hamiltonian is

$$H_A = \frac{\Omega}{2}\sigma^x + k_0(\alpha\sigma^y + \beta\sigma^z) \approx \frac{\Omega}{2}\sigma^x \quad (\text{A9})$$

(Recall that Ω is the Larmor frequency $\Omega = \mu_B g B$.) We ignore the slight perturbation to the spin Hamiltonian due to the coherent part of the spin-orbit coupling.

The correlation function $S_{\delta k}(\omega)$ must satisfy the KMS relation [65–67] (cf App. A.3)

$$S_{\delta k}(-\omega) = e^{-\beta\omega} S(\omega), \quad (\text{A10})$$

have a correlation time τ_k , and have a single-time variance

$$mT = \langle \delta k^2 \rangle = \int \frac{d\omega}{2\pi} S(\omega). \quad (\text{A11})$$

In the fast-decay limit $T \ll \tau_k^{-1}$

We take

$$S(\omega) = mT \frac{4\tau_k}{1 + (\omega\tau_k)^2} \frac{1}{1 + e^{-\omega/T}}. \quad (\text{A12})$$

To arrive at this form we take an exponential-in-time correlation decay $\langle \delta k(t)\delta k(0) \rangle = mT e^{t/\tau_k}$ and convolve it with a filter that enforces the KMS relation (A10); the KMS relation is more transparent if we write the spectral function in the equivalent form

$$S(\omega) = mT \frac{2\tau_k}{1 + (\omega\tau_k)^2} \frac{e^{\omega/2T}}{\cosh \omega/2T}. \quad (\text{A13})$$

This spectral function gives

$$\begin{aligned} \langle \delta k^2 \rangle &= \int_{-\infty}^{\infty} \frac{d\omega}{2\pi} S(\omega) \\ &= \begin{cases} mT & \text{fast decay } T \ll \tau_k^{-1} \\ \frac{1}{2}mT & \text{slow decay } T \gg \tau_k^{-1} \end{cases} \end{aligned} \quad (\text{A14})$$

We are in the fast-decay regime: for our devices

$$\begin{aligned} T &\sim 30 \text{ mK} \approx 4 \text{ GHz} \\ \tau_k^{-1} &\approx 100 \text{ GHz}. \end{aligned} \quad (\text{A15})$$

Moreover the factor of two difference is smaller than other sources of uncertainty and device-dependence in our calculation, in particular the spin orbit couplings α, β . We therefore do not calculate the interpolating T -dependence in the correlation function (A12).

The Lindblad master equation, then is

$$\begin{aligned} d_t \rho &= S_{\delta k}(\Omega)\alpha^2 \left[\sigma^- \rho \sigma^+ - \frac{1}{2} \{ \sigma^+ \sigma^-, \rho \} \right] \\ &+ S_{\delta k}(-\Omega)\alpha^2 \left[\sigma^+ \rho \sigma^- - \frac{1}{2} \{ \sigma^- \sigma^+, \rho \} \right] \\ &+ S_{\delta k}(0)\beta^2 [\sigma^z \rho \sigma^z - \rho] \end{aligned} \quad (\text{A16})$$

where $S_{\delta k}$ is the correlation function of (A12). It is convenient to identify rates

$$\begin{aligned} \Gamma_1 &= \Gamma_{1-} = S_{\delta k}(\Omega)\alpha^2 \\ \Gamma_{1+} &= S_{\delta k}(-\Omega)\alpha^2 \\ \Gamma_2 &= S_{\delta k}(0)\beta^2; \end{aligned} \quad (\text{A17})$$

these are the rates we quote in Eq. 20 in the main text. The T_1 and T_2 times are

$$\begin{aligned} \frac{1}{T_1} &\approx \alpha^2 S(\Omega) \approx \alpha^2 mT \frac{4\tau_k}{1 + (\Omega\tau_k)^2} \\ \alpha^2 S(-\Omega) &\approx \alpha^2 mT \frac{4\tau_k}{1 + (\Omega\tau_k)^2} e^{-\Omega/T} \\ \frac{1}{T_2} &= \beta^2 S(0) = 2mT\beta^2 \end{aligned} \quad (\text{A18})$$

where we have used that $\Omega/T \gg 1$ to simplify the KMS parts of (A12), and to ignore the contribution of $\downarrow \rightarrow \uparrow$ processes to T_1 .

A.3. KMS relation

The KMS relation is a basic feature of Gibbs-state correlation functions. In the time domain, a correlation function is

$$\langle A(t)A(0) \rangle = \text{Tr} e^{-iHt} A e^{iHt} A e^{-\beta H} \quad (\text{A19})$$

so

$$\begin{aligned} \langle A(-t)A(0) \rangle &= \text{Tr} e^{iHt} A e^{-iHt} A e^{-\beta H} \\ &= \text{Tr} e^{\beta H} e^{-iHt} A e^{iHt} e^{-\beta H} A e^{-\beta H} \\ &= \text{Tr} e^{-iH(t+i\beta)} A e^{iH(t+i\beta)} A e^{-\beta H} \\ &= \langle A(t+i\beta)A(0) \rangle \end{aligned} \quad (\text{A20})$$

where in the second line we have inserted $1 = e^{-\beta H} e^{\beta H}$ and used the cyclic property of the trace. (Note that here $\beta = 1/T$.) Taking a Fourier transform leads to

$$S(-\omega) = e^{-\beta\omega} S(\omega), \quad (\text{A21})$$

the form used in App. A.2.

A.4. Kraus operators of resulting channel

In App. A.2 we argued that spin-orbit coupling leads to a Lindblad dynamics for the spin

$$\begin{aligned} d_t \rho &= (\mathcal{L}_1 + \mathcal{L}_2) \rho \\ \mathcal{L}_1 \rho &= \Gamma_1 \left(\sigma^- \rho \sigma^+ - \frac{1}{2} \{P_\uparrow, \rho\} \right) \\ \mathcal{L}_2 \rho &= \Gamma_2 (\sigma^x \rho \sigma^x - \rho). \end{aligned} \quad (\text{A22})$$

Recall that our quantization axis is x , so $\sigma^\pm = \sigma^y \pm i\sigma^z$. As in A.2 we are ignoring the σ^+ transition, because it is suppressed by a factor of $e^{-\Omega/T}$ compared to the other terms.

In this subsection we rehearse a standard calculation for the Kraus operators of the channel given by evolution under this channel for time $t = L/v$. To find those operators, we compute the action of $e^{(\mathcal{L}_1 + \mathcal{L}_2)t}$ on the basis operators $\sigma^x, \sigma^y, P_\uparrow, P_\downarrow$, and then write Kraus operators that reproduce that action.

a. Action of Lindblad evolution on basis operators

Since

$$\begin{aligned} \mathcal{L}_1 \sigma^{y,z} &= -\frac{1}{2} \Gamma_1 \sigma^{y,z} \\ \mathcal{L}_1 P_\uparrow &= -\Gamma_1 (P_\uparrow - P_\downarrow) \\ \mathcal{L}_1 P_\downarrow &= 0 \end{aligned} \quad (\text{A23})$$

and

$$\begin{aligned} \mathcal{L}_2 \sigma^{y,z} &= -2\Gamma_2 \sigma^{y,z} \\ \mathcal{L}_2 P_{\uparrow,\downarrow} &= 0, \end{aligned} \quad (\text{A24})$$

the two Lindblad (super)operators commute, and we can treat them separately. Immediately

$$(\mathcal{L}_1 + \mathcal{L}_2) \sigma^{y,z} = -\left(\frac{1}{2} \Gamma_1 + 2\Gamma_2 \right) \sigma^{y,z} \quad (\text{A25})$$

so

$$e^{(\mathcal{L}_1 + \mathcal{L}_2)t} \sigma^{y,z} = e^{-(\frac{1}{2}\Gamma_1 + 2\Gamma_2)t} \sigma^{y,z} \quad (\text{A26})$$

from which we can read off

$$\frac{1}{T_2} = \frac{1}{2} \Gamma_1 + 2\Gamma_2. \quad (\text{A27})$$

The action on $P_{\uparrow,\downarrow}$ is less straightforward. Only \mathcal{L}_1 acts nontrivially. Immediately

$$\mathcal{L}_1^n P_\downarrow = 0, \quad (\text{A28})$$

and one can show

$$\mathcal{L}_1^n P_\uparrow = (-\Gamma_1)^n (P_\uparrow - P_\downarrow) \quad (\text{A29})$$

so

$$\begin{aligned} e^{\mathcal{L}_1 t} P_\downarrow &= \sum_n \frac{t^n}{n!} \mathcal{L}_1^n P_\downarrow = P_\downarrow \\ e^{\mathcal{L}_1 t} P_\uparrow &= \sum_n \frac{t^n}{n!} \mathcal{L}_1^n P_\uparrow = e^{-\Gamma_1 t} P_\uparrow + (1 - e^{-\Gamma_1 t}) P_\downarrow. \end{aligned} \quad (\text{A30})$$

from which we can read off

$$\frac{1}{T_1} = \Gamma_1. \quad (\text{A31})$$

Substituting now $t = L/v$ we find that the channel acts by

$$\begin{aligned} \sigma^{y,z} &\mapsto e^{-L/L_2} \sigma^{y,z} \\ P_\uparrow &\mapsto e^{-L/L_1} P_\uparrow + (1 - e^{-L/L_2}) P_\downarrow \\ P_\downarrow &\mapsto P_\downarrow \end{aligned} \quad (\text{A32})$$

with

$$\frac{1}{L_1} = \frac{1}{vT_1} = \frac{\Gamma_1}{v} \quad (\text{A33})$$

$$\frac{1}{L_2} = \frac{1}{vT_2} = \frac{1}{v} \left(\frac{1}{2} \Gamma_1 + 2\Gamma_2 \right). \quad (\text{A34})$$

These are the lengths we quote in the main text (Eq's (6) and (22)).

b. Channel and Kraus operators

It is easiest to back out the channel we seek as the composition of two channels:

- \mathcal{D}_1 with Kraus operators $a\sigma^-, bP_\uparrow + cP_\downarrow$, with the constants $0 \leq a, b, c \leq 1$ chosen so

$$\begin{aligned} \mathcal{D}P_\uparrow &= e^{-\Gamma_1 t} P_\uparrow + (1 - e^{-\Gamma_1 t}) P_\downarrow \\ \mathcal{D}P_\downarrow &= P_\downarrow \\ \mathcal{D}\sigma^{y,z} &= e^{-\frac{1}{2}\Gamma_1 t} \sigma^{y,z} \end{aligned} \quad (\text{A35})$$

- \mathcal{D}_2 with Kraus operators $dI, f\sigma^x$, with the constants chosen so

$$\begin{aligned} \mathcal{D}_2 P_{\uparrow,\downarrow} &= P_{\uparrow,\downarrow} \\ \mathcal{D}_2 \sigma^{y,z} &= e^{-\Gamma_2 t} \sigma^{y,z} \end{aligned} \quad (\text{A36})$$

These obviously commute, so

$$\mathcal{D}_1 \mathcal{D}_2 = \mathcal{D}_2 \mathcal{D}_1 \quad (\text{A37})$$

implements the desired channel. One can check that the desired properties come about with

$$\begin{aligned} a^2 &= 1 - e^{-\Gamma_1 t} \\ b^2 &= e^{-\Gamma_1 t} \\ c^2 &= 1 \\ d^2 &= \frac{1}{2} (1 - e^{-\Gamma_2 t}) \\ f^2 &= \frac{1}{2} (1 + e^{-\Gamma_2 t}), \end{aligned} \quad (\text{A38})$$

or substituting again $t = L/v$

$$\begin{aligned} a^2 &= 1 - e^{-L/L_1} \\ b^2 &= e^{-L/L_1} \\ c^2 &= 1 \\ d^2 &= \frac{1}{2} (1 - e^{-L/L_2}) \\ f^2 &= \frac{1}{2} (1 + e^{-L/L_2}). \end{aligned} \quad (\text{A39})$$

In the first instance the channel we want has Kraus operators

$$\begin{aligned} K'_1 &= fa\sigma^- \\ K_2 &= f(bP_\uparrow + cP_\downarrow) \\ K_3 &= d\sigma^x(bP_\uparrow + cP_\downarrow) \\ &= (dbP_\uparrow - dcP_\downarrow) \\ K_4 &= da\sigma^x\sigma^- \\ &= -da\sigma^- \\ &\sim da\sigma^- \end{aligned} \quad (\text{A40})$$

where in the last line I've used that Kraus operators are equivalent under sign change. Since K'_1, K_4 are scalar multiples of each other and $f^2 + d^2 = 1$ we can write the channel with three Kraus operators

$$\begin{aligned} K_1 &= a\sigma^- \\ K_2 &= f(bP_\uparrow + cP_\downarrow) \\ K_3 &= d(bP_\uparrow - cP_\downarrow). \end{aligned} \quad (\text{A41})$$

Appendix B: Variable g -factor

Consider a 1D Hamiltonian

$$H = \sum \frac{p^2}{2m} + \frac{1}{2} \Omega(\hat{x}) \sigma^z. \quad (\text{B1})$$

The Larmor frequency $\Omega(x)$ is random per device and varies in space, hence its dependence on the operator \hat{x} . Write square brackets

$$[\cdot] \quad (\text{B2})$$

for the average over devices, i.e. realizations of the random Larmor frequencies Ω . Work in a rotating frame to null out the average Larmor frequency $[\Omega]$.

Now consider a state

$$|\psi_{xk}\rangle\langle\psi_{xk}| \otimes \rho, \quad (\text{B3})$$

$|\psi_{xk}\rangle$ a wavepacket with center x , momentum k , and length l_e . At leading order in Ω the effective dynamics on the spin state is

$$\begin{aligned} d_t \rho &= -i \frac{1}{2} \underbrace{\langle\psi_{xk}|\Omega(\hat{x})|\psi_{xk}\rangle}_{\equiv \Omega_x} [\sigma^z, \rho] \\ &= -i \Omega_x [\sigma^z, \rho]. \end{aligned} \quad (\text{B4})$$

The effective Larmor frequency is

$$\begin{aligned} \Omega_x &\equiv \langle\psi_{xk}|\Omega(\hat{x})|\psi_{xk}\rangle \\ &= \int dx' |\psi_{xk}(x')|^2 \Omega(x'). \end{aligned} \quad (\text{B5})$$

B.1. Properties of Larmor frequency disorder

Assuming the wavepacket is Gaussian with width l_e and the function $\Omega(\hat{x})$ is short-range correlated, the effective Larmor frequency is

$$\begin{aligned} [\Omega_x] &= 0 \\ [\Omega_x \Omega_{x'}] &= \sigma_\Omega^2 e^{-(x-x')^2/2l_c}, \end{aligned}$$

for some variance σ_Ω^2 and correlation length $l_c = 2l_e$. Some later calculations are more transparent if we take Ω_x to have exponential, rather than Gaussian, correlations

$$[\Omega_x \Omega_{x'}] = \sigma_\Omega^2 e^{-|x-x'|/l_c}. \quad (\text{B6})$$

We expect the difference between exponential and Gaussian correlations to be small compared to the other approximations we are making.

The variance σ_Ω^2 is a key parameter. It is central-limiting, because (B5) is an average over a length l_e , as well as a width w . So

$$\sigma_\Omega^2 = \frac{\sigma_0^2}{wl_e}, \quad (\text{B7})$$

where σ_0^2 is a real device property. Since we assuming no magnetic field gradients, the Larmor frequency variation comes from g -factor variation; we can use dot-to-dot variation in the g factor to estimate σ_0 .

We expect σ_0 to correspond to a dot-to-dot g -factor variation $\Delta g/g \sim 10^{-4}$, based on experiments in SiMOS [81] and SiGe [54, 82], but it may be as large as 10^{-3} .

[81] measured $\Delta g/g \sim 10^{-3}$ in SiMOS devices. Since the g -factor variation is proportional to the SOC variation and SOC is roughly an order of magnitude larger in SiMOS devices than in the SiGe devices we consider, this result suggests $\Delta g/g \sim 10^{-4}$ for SiGe. The dots of [81] are $\sim 50 \text{ nm} \times 50 \text{ nm}$ [81][Suppl. Fig. 1].

[82], working in SiGe, do not cite a dot-to-dot g -factor difference, but their results can be used to estimate an upper. Instead they attribute the difference in Larmor frequencies to hyperfine interaction with nuclear spins in their devices, which are made with natural silicon. They see a standard deviation $\sigma_{HF} = 2.6 \text{ neV}$, consistent with a priori calculations for the effect of nuclear spins. Since they work at 30 mT, the Zeeman energy is $\approx 3.5 \text{ neV} \sim 10^3 \sigma_{HF}$, suggesting $\Delta g/g < 10^{-3}$ consistent with our estimate $\Delta g/g \sim 10^{-4}$. Their electron wavefunctions are somewhat smaller than $50 \text{ nm} \times 50 \text{ nm}$ [82][Fig. 1].

[54] measure the difference between the g -factors in two valleys, rather than two dots, and find $\Delta g/g \sim 10^{-4}$. We expect this to be a reasonable proxy for dot-to-dot variation: the g -factor difference is driven by an SOC difference, which is in turn driven by alloy disorder at the interface, and the two valley states see different portions of the interface alloy disorder.

The result is

$$\sigma_0^2 \sim l_{\text{dot}}^2 [\Omega_0 \Delta g/g]^2 \approx (0.44 \text{ GHz} \cdot \text{nm})^2 . \quad (\text{B8})$$

B.2. Properties of electron motion

We assume the electron follows a random walk ξ_t with diffusion coefficient

$$D = T\mu/e \approx (160 \text{ nm})^2/\text{ns} . \quad (\text{B9})$$

and drift

$$v_0 = \mu E = 1000 \text{ m/s} , \quad (\text{B10})$$

so the probability that it is at position x at time t given that it was at position 0 at time 0 is given by the propagator

$$P(\xi_t = x | \xi_0 = 0) = e^{-(x-vt)^2/2Dt} \quad (\text{B11})$$

Drift becomes more important than diffusion on length-scales larger than

$$l_D = D/v_0 \approx 26 \text{ nm} . \quad (\text{B12})$$

Concretely, from (B11) one can see that once the electron has travelled more than [a few] $\cdot l_D$, it is unlikely to return

to its starting position. On lengthscales long compared to l_D , then, we should think of the electron as primarily following the deterministic drift velocity.

Write

$$\langle \cdot \rangle \quad (\text{B13})$$

for the average over ξ , i.e. electron paths in single device.

B.3. Computing decoherence

Suppose the center of the electron wavepacket follows a random walk ξ_t in the channel. The electron acquires a total z rotation angle

$$\begin{aligned} \theta &= \int_0^\infty dt \Omega_{\xi_t} \\ &= \int_0^\infty dt \int_0^L dx \Omega_x \delta(x - \xi_t) . \end{aligned} \quad (\text{B14})$$

where we take $\Omega = 0$ in the target dot. (Recall Ω is actually the noise around some nominal value.) The average over electron paths for a single device is

$$\begin{aligned} \langle \theta \rangle &= \int_0^\infty dt \int_0^L dx \Omega_x \langle \delta(x - \xi_t) \rangle \\ &= \int_0^\infty dt \int_0^L dx \Omega_x P(\xi_t = x | \xi_0 = 0) \\ &= \frac{1}{v_0} \int_0^L dx \Omega_x \end{aligned} \quad (\text{B15})$$

$$\langle \theta \rangle^2 = \frac{1}{v_0^2} \int_0^L dx dx' \Omega_x \Omega_{x'} . \quad (\text{B16})$$

where the last step in the $\langle \theta \rangle$ calculation follows by interchanging integrals and using the diffusion time integral (C3). The device average is

$$[\langle \theta \rangle] = \frac{1}{v_0} \int_0^L dx [\Omega_x] = 0 . \quad (\text{B17})$$

The second moment of the rotation angle is

$$\begin{aligned} \langle \theta^2 \rangle &= \int_0^L dx dx' \Omega_x \Omega_{x'} \int_0^\infty dt dt' \langle \delta(x - \xi_t) \delta(x' - \xi_{t'}) \rangle \\ &= \int_0^L dx dx' \Omega_x \Omega_{x'} G(x, x') . \end{aligned} \quad (\text{B18})$$

Here

$$\begin{aligned}
G(x, x') &= \int_0^\infty dt dt' \langle \delta(x - \xi_t) \delta(x' - \xi_{t'}) \rangle \\
&= \int_0^\infty dt \int_0^\infty d\tau \langle \delta(x - \xi_t) \delta(x' - \xi_{t+\tau v}) \rangle \\
&\quad + (x \leftrightarrow x') \\
&= \left[\int_0^\infty dt P(\xi_\tau = x' - x | \xi_0 = 0) \right] \\
&\quad \times \left[\int_0^\infty d\tau P(\xi_t = x' | \xi_0 = 0) \right] + (x \leftrightarrow x') \\
&= \frac{1}{v_0^2} \left\{ \begin{array}{ll} e^{-2|x-x'|} & x' < x \\ 1 & x' > x \end{array} \right\} + (x \leftrightarrow x') \\
&= \frac{1}{v_0^2} \left[1 + e^{-2|x-x'|/l_c} \right]. \tag{B19}
\end{aligned}$$

using the diffusion time integral of App. C Now the second moment is

$$\begin{aligned}
\langle \theta^2 \rangle &= \frac{1}{v_0^2} \int_0^L dx dx' \Omega_x \Omega_{x'} \left[1 + e^{-2|x-x'|/l_c} \right] \\
&= \langle \theta \rangle^2 + \frac{1}{v_0^2} \int_0^L dx dx' \Omega_x \Omega_{x'} e^{-2|x-x'|/l_c}. \tag{B20}
\end{aligned}$$

for a variance

$$\langle \theta^2 \rangle - \langle \theta \rangle^2 = \frac{1}{v_0^2} \int_0^L dx dx' \Omega_x \Omega_{x'} e^{-2|x-x'|/l_c}. \tag{B21}$$

The average *over devices* of the variance *over shots per device* is

$$\begin{aligned}
\left[\langle \theta^2 \rangle - \langle \theta \rangle^2 \right] &= \frac{1}{v_0^2} \int_0^L dx dx' [\Omega_x \Omega_{x'}] e^{-2|x-x'|/l_c} \\
&\approx L \frac{2\sigma_\Omega^2 l_c}{v_0^2} \sqrt{2\pi} e^{4l_c^2/l_D^2} \operatorname{erfc}(2l_c/l_D) \quad [\text{Gaussian}] \\
&\approx L \frac{2\sigma_\Omega^2}{v_0^2} [1/l_c + 2/l_D]^{-1} \quad [\text{exponential}] \tag{B22}
\end{aligned}$$

depending on whether the noise has exponential or Gaussian correlations in space. assuming $l_D, l_c \ll L$. The Gaussian case can be treated with the small- x Taylor and large- x asymptotic expansions of erfc

$$\operatorname{erfc} x \approx \begin{cases} 1 - \frac{2}{\sqrt{\pi}} x & x \ll 1 \\ \frac{1}{x\sqrt{\pi}} e^{-x^2} & x \gg 1. \end{cases} \tag{B23}$$

Since this is somewhat opaque, we instead consider exponential correlations, from which we can read off a decoherence length

$$L_2 = \frac{v_0^2}{\sigma_\Omega^2 l_D} [1 + l_c/2l_D]. \tag{B24}$$

Appendix C: Diffusion time integral

We repeatedly come up against the integral

$$\begin{aligned}
&\int_0^\infty dt P(\xi_t = x | \xi_0 = 0) \\
&= \int_0^\infty dt \frac{1}{\sqrt{2\pi Dt}} \exp \left[-\frac{(x-vt)^2}{2Dt} \right]. \tag{C1}
\end{aligned}$$

To do the integral change variables

$$\begin{aligned}
u &= \frac{v}{D} x \\
y &= \frac{v^2}{D} t \tag{C2}
\end{aligned}$$

for

$$\begin{aligned}
&\int_0^\infty dt P(\xi_t = x | \xi_0 = 0) \\
&= \int_0^\infty dt \frac{1}{\sqrt{2\pi Dt}} \exp \left[-\frac{(x-vt)^2}{2Dt} \right] \\
&= \frac{1}{v} \int_0^\infty \frac{dy}{\sqrt{2\pi y}} e^{-(u-y)^2/2y} \\
&= \frac{1}{v} \begin{cases} e^{-2|x|} & x < 0 \\ 1 & x > 0. \end{cases} \tag{C3}
\end{aligned}$$

Appendix D: Nuclear spin impurities

D.1. Elementary calculation of dephasing by a single impurity, ignoring electric field and momentum scattering

Consider an electron and a single nuclear spin, with the nuclear spin located (for convenience) at $x = 0$. Take the initial state of the combined system, at some $t_{init} \ll 0$, to be

$$\begin{aligned}
\rho(t_{init}) &= \rho_0 \\
&= \rho_n \rho_s \otimes \int dx dk p(x) p(k) |\psi(x, k)\rangle \langle \psi(x, k)| \tag{D1}
\end{aligned}$$

where ρ_n, ρ_s are the nucleon and electron spin states the electron spin state,

$$|\psi(x, k)\rangle = \int dx' e^{-ikx} e^{-(x'-x)^2/4l_e^2} |x'\rangle \tag{D2}$$

is a wavepacket with position $\sim x$, momentum $\sim k$, and width l_e ,

$$p(k) \propto e^{-\frac{(k-k_0)^2}{2mT}} \tag{D3}$$

is the Gibbs distribution for momentum, and $p(x)$ is some initial distribution of wavepacket midpoints. We assume that $p(x)$ is nontrivial only for $x \ll -l_e$, so the wavepackets start well to the left of the impurity.

The system has a Hamiltonian

$$H = \underbrace{\frac{\hat{k}^2}{2m}}_{\equiv K} + \underbrace{au\delta(\hat{x})\boldsymbol{\sigma}_e \cdot \boldsymbol{\sigma}_n}_{\equiv V}. \quad (\text{D4})$$

(We hat the position and momentum operators \hat{x}, \hat{k} to distinguish them from the various other position and momentum variables.)

Estimate the electron spin density matrix long after it passes the nuclear spin by treating treating the interaction V as a perturbation, working in the interaction picture, and tracing out the nuclear spin and momentum degrees of freedom. The full density matrix (of all three degrees of freedom, electron spin, nuclear spin, and electron momentum) is

$$\begin{aligned} \rho(t = \infty) &= \rho_0 - i \int_{-\infty}^{\infty} dt [V_I(t), \rho_0] \\ &\quad - \int_{-\infty}^{\infty} dt \int_{-\infty}^t dt' [V_I(t), [V_I(t'), \rho_0]] \end{aligned} \quad (\text{D5})$$

where we have extended the lower integration limit from t_{init} to $-\infty$. Performing the trace, the individual terms are

$$\begin{aligned} \text{Tr}_{k,n}[V_I(t), \rho_0] &= au \int dx dk p(x)p(k) \langle \psi_{xk} | \delta(\hat{x}(t)) | \psi_{xk} \rangle \\ &\quad \times \text{Tr}_n[\boldsymbol{\sigma}_n \cdot \boldsymbol{\sigma}_e \rho_n \rho_s] \\ &= 0 \end{aligned} \quad (\text{D6})$$

because $\text{Tr} \sigma^j \rho_n = 0$, and

$$\begin{aligned} \text{Tr}[V_I(t)[V_I(t'), \rho_0]] &= (au)^2 \left[\int dx dk \langle \psi_{xk} | \delta(\hat{x}(t)) \delta(\hat{x}(t')) | \psi_{xk} \rangle + h.c. \right] \\ &\quad \times (\rho_s - \sigma^z \rho_s \sigma^z) \end{aligned} \quad (\text{D7})$$

where for now we are ignoring the relaxation terms σ^x, σ^y in the interaction.

To compute the overlap $\langle \psi_{xk} | \delta(\hat{x}(t)) \delta(\hat{x}(t')) | \psi_{xk} \rangle$ note that $|\psi_{xk}\rangle$ is in a subspace very close to momentum k . Ignoring dispersion, then,

$$\hat{x}(t) \approx \hat{x} + (k/m)t, \quad (\text{D8})$$

so

$$\begin{aligned} &\langle \psi_{xk} | \delta(\hat{x}(t)) \delta(\hat{x}(t')) | \psi_{xk} \rangle \\ &= \int dx' dx'' \psi_{xk}(x')^* \langle x' | \delta(\hat{x} + vt) \delta(\hat{x} + vt' | x'') \psi_{xk}(x'') \\ &= \int dx' dx'' \psi_{xk}(x')^* \langle x' | x'' \rangle \delta(x'' + vt) \delta(x'' + vt') \\ &= |\psi_{xk}(-vt)|^2 \delta(vt - vt') \\ &= |\psi_{xk}(-vt)|^2 v^{-1} \delta(t - t'). \end{aligned} \quad (\text{D9})$$

where $v = k/m$. Now

$$\text{Tr}[V_I(t)[V_I(t'), \rho_0]] = \frac{m(au)^2}{k} \delta(t - t') (\rho_s - \sigma^z \rho_s \sigma^z) \quad (\text{D10})$$

and the $t = \infty$ electron spin state is

$$\begin{aligned} \rho_s(t = \infty) &= \rho_s(0) - \int dx dk p(x)p(k) \int_{-\infty}^{\infty} dt \int_{-\infty}^t dt' \delta(t - t') \\ &\quad \times |\psi_{xk}(-k/m \cdot t)|^2 \frac{m(au)^2}{k} (\rho_s - \sigma^z \rho_s \sigma^z) \\ &= \int dk p(k) [(1 - \Gamma_k) \rho_s(0) + \Gamma_k \rho_s(0)] \end{aligned} \quad (\text{D11})$$

The position integral is trivial—physically this came about because every wavepacket eventually encounters, or has encountered, the nuclear spin, and we assume that position and momentum are uncorrelated. We therefore drop it. We have identified a momentum-dependent dephasing probability

$$\begin{aligned} \Gamma_k &= \int_{-\infty}^{\infty} dt \int_{-\infty}^t dt' \delta(t - t') |\psi_{xk}(-k/m \cdot t)|^2 \frac{m(au)^2}{k} \\ &= \left(\frac{mau}{k} \right)^2. \end{aligned} \quad (\text{D12})$$

This naturally agrees with the momentum-dependent dephasing probability estimated in the main text, which followed the same logic. It also agrees with a scattering theory calculation in App. D.3.

D.2. Elementary calculation of dephasing by a single impurity, with random walk

In App. D.1 we assumed that a wavepacket $|\psi_{xk}\rangle$ coasted along with speed $v = k/m$ in the unperturbed (KE-only) dynamics. That dynamics gave an interaction-picture position operator

$$\hat{x}(t) = \hat{x} + \xi_t, \quad \xi = (k/m)t, \quad (\text{D13})$$

where ξ_t was the amount the wavepacket had moved. This ignored both momentum relaxation and the effect of the electric field.

To account for the effect of momentum scattering and electric field we now assume that the wavepacket follows a random walk (Wiener process with drift) with average speed $v_0 = \mu E$ and diffusion coefficient given by an Einstein relation $D = T\mu/e$; for our model device these are $v_0 = 1 \mu\text{m/ns}$ and $D \approx (160 \text{ nm})^2/\text{ns}$. This random walk model is reasonable on timescales $t \gg \tau_k$ the momentum relaxation time. In this model ξ_t , the amount the wavepacket has moved, is a Wiener process with drift.

Although we view the random walk primarily as a phenomenological description of the effect of momentum

relaxation and electric field, it can be justified microscopically. Translation-invariant scattering sources—e.g. phonon emission or scattering from conduction electrons in the resistive topgate—will give a Lindblad dynamics

$$d_t \rho = -i[K, \rho] \quad (\text{D14})$$

$$- \int dk \gamma_{k'k} \left[c_{k'}^\dagger c_k \rho - \frac{1}{2} \{n_k(1-n_k), \rho\} \right]$$

(or, equivalently, Boltzmann-equation dynamics for the momentum degree of freedom). $K = k^2/2m$ is the kinetic energy; $\gamma_{k'k}$ is the rate of scattering $k \rightarrow k'$; it depends on matrix elements with the scattering source, the scattering source temperature and density of states, etc. Non-translation-invariant scattering sources—e.g. impurities or alloy disorder

The Lindblad dynamics (D14) has many unravelings—that is, there are many different stochastic dynamics that give the same Lindblad equation on averaging. One convenient unraveling is random jumps

$$|\psi_{xk}\rangle \rightarrow |\psi_{xk'}\rangle \quad (\text{D15})$$

with rate $\gamma_{k'k}$. In Boltzmann language, this corresponds to sampling from the Boltzmann dynamics on the combined probability distribution $p(x, k)$. On timescales $t \gg \tau_k$ the relaxation time, these jumps lead to a random walk.

In this random walk picture the relevant matrix element is

$$\begin{aligned} & \langle \psi_{xk} | \delta(\hat{x}(t)) \delta(\hat{x}(t')) | \psi_{xk} \rangle \\ &= \int dx' dx'' \psi_{xk}(x')^* \langle x' | \delta(\hat{x} + \xi_t) \delta(\hat{x} + \xi_{t'} | x'') \psi_{xk}(x'') \\ &= \int dx' dx'' \psi_{xk}(x')^* \langle x' | x'' \rangle \delta(x'' + \xi_t) \delta(x'' + \xi_{t'}) \\ &= |\psi_{xk}(-\xi_t)|^2 \delta(\xi_t - \xi_{t'}) \end{aligned} \quad (\text{D16})$$

and so—for a particular random walk ξ !—the momentum-dependent dephasing probability is

$$\Gamma_k = (au)^2 \int_{-\infty}^{\infty} dt \int_{-\infty}^t dt' |\psi_{xk}(-\xi_t)|^2 \delta(\xi_{t'} - \xi_t).$$

But we also need to average over random paths ξ . The path average of the integrand can be re-written

$$\begin{aligned} & \langle |\psi_{xk}(-\xi_t)|^2 \delta(\xi_t - \xi_{t'}) \rangle \\ &= \int dx' |\psi_{xk}(x')|^2 \cdot P(\xi_t' = x' | \xi_{t_{init}} = 0) \\ & \quad \times P(\xi_t = x' | \xi_{t'} = x') \end{aligned} \quad (\text{D17})$$

In general, the the (time- and space-translation invariant) propagator of a Wiener process is

$$P(\xi_\tau = y | \xi_0 = 0) = \frac{1}{\sqrt{2\pi D\tau}} \exp \left[-\frac{(y - v\tau)^2}{2D\tau} \right], \quad (\text{D18})$$

so

$$P(\xi_t' = x' | \xi_{t_{init}} = 0) = \frac{1}{\sqrt{2\pi D(t' - t_{init})}} e^{x'^2/2D(t' - t_{init})}$$

$$P(\xi_t = x' | \xi_{t'} = x') = \frac{1}{\sqrt{2\pi D(t - t')}} e^{-v^2(t-t')/2D} \quad (\text{D19})$$

The latter is independent of x' —ultimately this is because the random walk is translation-invariant. So the matrix element is

$$\begin{aligned} & \langle |\psi_{xk}(-\xi_t)|^2 \delta(\xi_t - \xi_{t'}) \rangle \\ &= \frac{1}{\sqrt{2\pi D(t - t')}} e^{-v_0(t-t')/2D} \\ & \quad \times \int dx' |\psi_{xk}(x')|^2 \frac{1}{\sqrt{2\pi D(t' - t_{init})}} e^{x'^2/2D(t' - t_{init})} \end{aligned} \quad (\text{D20})$$

$$\quad (\text{D21})$$

The x' integral is easily estimated by noting that t_{init} is big, so most of the time $|\psi_{xk}(x')|^2$ is narrowly spread around $x' = x$, so and

$$\begin{aligned} & \langle |\psi_{xk}(-\xi_t)|^2 \delta(\xi_t - \xi_{t'}) \rangle \\ & \approx \frac{1}{\sqrt{2\pi D(t - t')}} e^{-v_0^2(t-t')/2D} \times P(\xi_{t'} = x | \xi_{t_{init}} = 0) \end{aligned} \quad (\text{D22})$$

Now

$$\begin{aligned} \Gamma_k &= (au)^2 \int_{t_{init}}^{\infty} dt P(\xi_{t'} = x | \xi_{t_{init}} = 0) \\ & \quad \times \int_0^{\infty} ds \frac{1}{\sqrt{2\pi Ds}} e^{-v_0^2 s/2D}. \end{aligned} \quad (\text{D23})$$

The s integral in the second line is easily seen to be

$$\int_0^{\infty} ds \frac{1}{\sqrt{2\pi Ds}} e^{-v_0^2 s/2D} = \frac{1}{v_0} \quad (\text{D24})$$

(change of variables, then recognize $\Gamma(1/2)$). The t integral is the diffusion time integral of App. C

$$\begin{aligned} & \int_{t_{init}}^{\infty} dt P(\xi_{t'} = x | \xi_{t_{init}} = 0) \\ &= \int_0^{\infty} d\tau \frac{1}{\sqrt{D\tau} \cdot 2\pi} \exp \left[-\frac{(x - v_0 t)^2}{2D\tau} \right] \\ &= \frac{1}{v_0}. \end{aligned} \quad (\text{D25})$$

Putting the integrals together gives the expected

$$\Gamma_k = \left(\frac{au}{v_0} \right)^2 = \left(\frac{au}{\mu E} \right)^2 \quad (\text{D26})$$

D.3. Scattering theory calculation of dephasing by a single impurity

Write $|k\rangle$ for an incoming wavepacket at momentum k ; $|L_k\rangle, |R_k\rangle$ are outgoing wavepackets (leftward and rightward) at momentum k ; and $\hat{R}_k^\sigma, \hat{T}_k^\sigma$ are the action on

the spin degree of freedom corresponding to reflection and transmission respectively. $\sigma = \pm 1$ labels the nuclear spin. In general the outgoing momenta do not have to match the incoming momenta. But the scattering is elastic, because we consider dephasing.

We again treat the hyperfine interaction as a perturbation. Consider an eigenstate of the unperturbed Hamiltonian (KE + Zeeman field)

$$|\phi\rangle = |kz\rangle, \quad (\text{D27})$$

where $z = \pm 1$ is an electron spin eigenvalue. This state has energy

$$E = \frac{k^2}{2m} - \frac{1}{2}\Omega z, \quad (\text{D28})$$

so the Green's function is

$$\begin{aligned} & [H_0 - E - i\epsilon]^{-1} \\ &= \int dk' \frac{2m}{k'^2 - k^2 - \frac{1}{2}\Omega(\sigma_e^z - z) - i\epsilon} |k'\rangle\langle k'| \end{aligned} \quad (\text{D29})$$

Then the first Born approximation is

$$\begin{aligned} |\psi\rangle &= \int dk' \frac{2m}{k'^2 - k^2 - B(\sigma_e^z - z) - i\epsilon} |k'\rangle\langle k'| \\ &\quad \times -ua\sigma_n^z \sigma_e^z |r=0\rangle\langle r=0| kz \end{aligned} \quad (\text{D30})$$

Since $\langle r=0|k\rangle = 1$, this is

$$\begin{aligned} |\psi\rangle &= |k\rangle - \int dk' \frac{2mua z}{k'^2 - k^2 - B(\sigma_e^z - z) - i\epsilon} |k'z\rangle \\ &= |k\rangle - \int dk' \frac{2mua z}{k'^2 - k^2 - i\epsilon} |k'z\rangle \end{aligned} \quad (\text{D31})$$

In real space this is

$$|\psi\rangle = \int dx \left[e^{ikx} + i \frac{muz}{k} e^{-ik|x|} \right] |xz\rangle \quad (\text{D32})$$

from which we can read off reflection and transmission matrices

$$\begin{aligned} \hat{R}_k &= i\sigma_n \frac{mua}{k} z \\ \hat{T}_k &= 1 - i\sigma_n \frac{mua}{k} z. \end{aligned} \quad (\text{D33})$$

The scattering rate mua/k diverges as $k \rightarrow 0$.

The scattering process takes

$$\begin{aligned} |k\rangle\langle k| \otimes \rho \mapsto \sum_{\sigma} \left[|L_k\rangle\langle L_k| \otimes \hat{R}_k^{\sigma} \rho \hat{R}_k^{\sigma\dagger} + |R_k\rangle\langle R_k| \otimes \hat{T}_k^{\sigma} \rho \hat{T}_k^{\sigma\dagger} \right] \\ + [\text{L-R cross terms}]. \end{aligned} \quad (\text{D34})$$

We assume that soon after scattering from the nuclear spin, the electron scatters again from non-magnetic impurities, from conduction electrons in the wire on top of

the channel, or from other scattering sources. That scattering renders the position/momentum degree of freedom incoherent, so the action on the spin degree of freedom is given by the partial trace, which is can be read off using the fact that all the $|L_k\rangle, |R_k\rangle$ are orthonormal. The partial trace—the effective action on the electron spin degree of freedom—is therefore

$$\rho \mapsto \int dk p_k \left[\hat{R}_k \rho \hat{R}_k^{\dagger} + \hat{T}_k \rho \hat{T}_k^{\dagger} \right]. \quad (\text{D35})$$

Averaging out the nuclear spin and recognizing z as the eigenstates of σ_e^z leaves

$$\begin{aligned} \rho \mapsto \int dk p_k \left[(1 - \Gamma_k) \rho + \Gamma_k \sigma^z \rho \sigma^z \right], \\ \Gamma_k = \left(\frac{mua}{k} \right)^2. \end{aligned} \quad (\text{D36})$$

D.4. Hyperfine interaction

a. Dipole-Dipole interaction with the nucleus

A magnetic impurity with nuclear spin \mathbf{I} (in our case $I = 1/2$) gives rise to a magnetic field

$$B(\mathbf{r}) = \frac{\mu_0}{4\pi} \left[\frac{3\hat{\mathbf{r}}(\hat{\mathbf{r}} \cdot \mathbf{m} - \mathbf{m})}{r^3} + \frac{8\pi}{3} \mathbf{m} \delta^3(\mathbf{r}) \right] \quad (\text{D37})$$

with $\mathbf{m} = \gamma_n \mathbf{I}$, γ_n the gyromagnetic ratio of the nucleus, and the nucleus at $\mathbf{r} = 0$. Experiments [83] show that the δ -function part dominates, so we can take this to be

$$B(\mathbf{r}) = \frac{2\mu_0}{3} \gamma_n \mathbf{I} \delta^3(\mathbf{r}). \quad (\text{D38})$$

[100] gives

$$\begin{aligned} \gamma_n &= -8.458 \text{ MHz/T} \cdot 2\pi\hbar \\ &\approx -35 \text{ neV/T} \end{aligned} \quad (\text{D39})$$

for the ^{29}Si gyromagnetic ratio.

The energy of an electron in this field is

$$\begin{aligned} E &= \int d^3\mathbf{r} |\psi(\mathbf{r})|^2 \mu_B z_e B_z(\mathbf{r}) \\ &= \frac{2\mu_0}{3} g\mu_B \gamma_n (z_e \sigma) |\psi(\mathbf{r})|^2 \end{aligned} \quad (\text{D40})$$

(assuming, as elsewhere in this note, that the nucleus is in a $\pm z$ spin eigenstate σ).

The question, now, is the wavefunction $|\psi(\mathbf{r})|^2$.

b. Effective mass theory: wavefunction on scales $r > a$

To predict the wavefunction at the level of unit cells—that is, with a “resolution” $r \gtrsim a$ the lattice constant—use effective mass theory: solve

$$E\psi(\mathbf{r}) = -\frac{1}{2m_\alpha} \frac{\partial^2}{\partial x_\alpha^2} \psi(\mathbf{r}) + V(\mathbf{r})\psi(\mathbf{r}). \quad (\text{D41})$$

We write ψ for the wavefunction at this resolution, which tells you how much amplitude is in each unit cell.

The potential varies with the physics under consideration. [101, 102], on which [83] leans, consider a single donor electron (e.g. P). (Feher goes on to use the bunching—App. c—to predict the hyperfine spitting of (D40) and compare to his experiments.) We will have in mind a hard-walled box in two directions, and an infinite extent in the third.

c. Bunching: wavefunction on scales short compared to lattice

The effective mass theory of tells us the amplitude in each unit cell, but we need the amplitude at the ^{29}Si site. This is given by the full wavefunction, which I’ll call $\psi(\mathbf{r})$: the wavefunction that describes the electron on scales comparable to an atomic covalent radius. We already have $\psi(\mathbf{R})$, \mathbf{R} the location of the spin impurity, from effective mass calculations. We would expect $\psi(\mathbf{r})$ at the impurity to scale with $\psi(\mathbf{r})$, so define the **bunching**

$$\eta = \frac{|\psi(\mathbf{r})|^2}{|\psi(\mathbf{R})|^2}. \quad (\text{D42})$$

In terms of the bunching, the energy of the electron is

$$E = \frac{2\mu_0}{3} g\mu_B \gamma_n \eta (z_e \sigma) |\psi(\mathbf{R})|^2 \quad (\text{D43})$$

The precise value of the bunching factor is in some doubt. [84] measure it at

$$\eta = 186 \pm 18 \quad [\text{Shulman and Wyluda}]; \quad (\text{D44})$$

this is what Feher uses. [85] claims that Shulman and Wyluda made two roughly countervailing errors—a factor of 2 mistake and an incorrect mobility—and quotes unpublished work of I. Solomon as giving

$$\eta = 178 \quad [\text{Solomon}]. \quad (\text{D45})$$

(see Ref’s [31, 32] of [85].) Knight shift measurements of [86] in phosphorus- and boron-doped Si give

$$\eta = 100 \pm 10 \quad [\text{Sundfors; P}] \quad (\text{D46a})$$

$$\eta = 80 \pm 10 \quad [\text{Sundfors; B}] \quad (\text{D46b})$$

(table V). DFT calculations of [87] and [88] give

$$\eta = 159.4 \pm 4.5 \quad [\text{Assali et al.}] \quad (\text{D47a})$$

$$\eta = 88 \quad [\text{Philippopoulos et al.}] \quad (\text{D47b})$$

We take

$$\eta = 100. \quad (\text{D48})$$

d. “Effective mass theory” for our channel

We have in mind a long wire with width $w \approx 100$ nm and thickness $b = 10$ nm.

To get to a 1+1d effective model, factorize the (effective mass theory) wavefunction

$$\psi(\mathbf{r}) = \psi_x(x)\psi_y(y)\psi_z(z) \quad (\text{D49})$$

with x along the wire and z transverse to the Si layer. The x and y factors will be roughly

$$\psi_x \sim 1/\sqrt{w} \quad (\text{D50a})$$

$$\psi_y \sim 1/\sqrt{b}, \quad (\text{D50b})$$

so the energy (D43) becomes

$$\begin{aligned} E &= \frac{2\mu_0}{3} g\mu_B \gamma_n \eta (z_e \sigma) |\psi_x|^2 |\psi_y|^2 |\psi_z(0)|^2 \\ &= \frac{2\mu_0}{3} \frac{g\mu_B \gamma_n \eta}{wb} (z_e \sigma) |\psi_z(0)|^2 \end{aligned} \quad (\text{D51})$$

from which we can read off the parameters au

$$au = \frac{2\mu_0}{3} \frac{g\mu_B \gamma_n \eta}{wb}. \quad (\text{D52})$$

D.5. Nuclear spin contribution to the Larmor frequency landscape

The ^{29}Si nuclear spins give an Overhauser magnetic field resulting in a contribution to the electron Larmor frequency

$$\Omega_{\text{nucl}} = \sum_j \sigma_j au |\psi(x_j)|^2 \quad (\text{D53})$$

where the sum is over nuclear spin impurities. The variance is

$$\sigma_{\Omega_{\text{nucl}}}^2 = \text{var } \Omega_{\text{nucl}} \sim a^2 u^2 (wb\nu) / l_e \quad (\text{D54})$$

using that $|\psi(x_j)|^2 \sim 1/l_e$ on a length scale of l_e , from which we can back out a variance per unit area

$$\sigma_{0;\text{nucl}} \sim a^2 u^2 w^2 b \nu = \left(\frac{2\mu_0}{3} g\mu_B \gamma_n \eta \right)^2 \frac{1}{b} \nu. \quad (\text{D55})$$

Returning to the results of App. B, this gives

$$\begin{aligned} L_2^{-1} &\sim \frac{\sigma_{0;\text{nucl}}^2 T}{e l_e w \mu^2 E^3} \\ &= \left(\frac{2\mu_0}{3} \frac{g\mu_B \gamma_n \eta}{\mu E} \right)^2 \frac{\nu}{wb} \frac{T}{e E l_e} \end{aligned} \quad (\text{D56})$$